Scalable Effective Models for Superconducting Nanostructures: Applications to Double, Triple, and Quadruple Quantum Dots

Daniel Bobok, ¹ Lukáš Frk, ¹ Vladislav Pokorný, ² and Martin Žonda ¹ Department of Condensed Matter Physics, Faculty of Mathematics and Physics, Charles University, Ke Karlovu 5, Praha 2 CZ-121 16, Czech Republic ² Institute of Physics (FZU), Czech Academy of Sciences,

Na Slovance 2, 182 00 Prague 8, Czech Republic

We introduce a versatile and scalable framework for constructing effective models of superconducting (SC) nanostructures described by the generalized SC Anderson impurity model with multiple quantum dots and leads. Our Chain Expansion (ChE) method maps each SC lead onto a finite tight-binding chain with parameters obtained from Padé approximants of the tunneling self-energy. We provide an explicit algorithm for the general case as well as simple analytical expressions for the chain parameters in the wide-band and infinite-chain limits. This mapping preserves low-energy physics while enabling efficient simulations; short chains are tractable using exact diagonalization, and longer ones are handled with density matrix renormalization group methods. The approach remains reliable and computationally efficient across diverse geometries, both in and out of equilibrium. We use ChE to map the ground-state phase diagrams of double, triple, and quadruple quantum dots coupled to a single SC lead. While half-filled symmetric systems show similar overall diagrams, the particular phases differ substantially with the dot number. Here, large parameter regions are entirely missed by the widely used zero-bandwidth approximation but are captured by ChE. Away from half-filling, additional dots markedly increase diagram complexity, producing a rich variety of stable phases. These results demonstrate ChE as a fast, accurate, and systematically improvable tool for exploring complex SC nanostructures.

I. INTRODUCTION

In the last decades, significant progress has been achieved in experimental techniques that allow for coupling nanodevices with only a few active orbitals, here called quantum dots (QDs) for simplicity, with superconducting (SC) reservoirs [1–3]. Consequently, the overall complexity of these experimental systems increases steadily. Junctions, where SC leads are bridged by effective QDs, have been prepared in multi-lead arrangements [4, 5]. Tunable double quantum dots (DQDs) have been constructed in serial [6–8] as well as parallel [9, 10] configurations. The scanning tunneling microscopy (STM) and spectroscopy (STS) experiments, where QDs are placed on SC surface are already probing dimers [11–17] and more complicated setups [18– 23. They promise future applications in superconducting electronics, spintronics, and other computational devices, and represent tunable platforms for basic research [1– 3, 24-26].

Naturally, this progress also motivates advances in the theoretical study of complex QD-SC systems. The paradigmatic framework for describing such setups is the SC Anderson impurity model (SC-AIM), which involves one or more impurity levels [27]. Interestingly, even the simplest case of a single QD coupled to a single SC lead remains an active area of research [28, 29]. For instance, it has only recently been shown that a Kondo cloud screens the impurity spin even in the presence of an SC gap [30], and methods for treating non-equilibrium phenomena are still under active development [31, 32]. More complex configurations – such as DQDs or multiple leads – have already revealed unexpected features,

including previously unaccounted-for phases [33–35] and overlooked symmetries [36–38], and serve as a basis for recent qubit proposals [24, 39].

As one proceeds to even more complex structures, now commonly addressed in experiments, reliable numerical methods such as numerical renormalization group (NRG) [33, 40–47] or various types of quantum Monte Carlo [48–52] becomes too expensive even in equilib-In certain regimes, a feasible alternative are analytic approximations, e.g., various mean-field approaches [41, 53–56], perturbation expansions [57–61], and functional renormalization group techniques [62, 63]. Another strategy is to use simple effective models, such as the zero-bandwidth approximation (ZBW) [8, 58] and the SC atomic limit (AL) [27]. Their great advantage is that they can be exactly solvable even in complex scenarios. However, ZBW and AL are limited to qualitative description [27, 33]. For AL, this problem can be mitigated to a large extent by generalized AL (GAL) [34, 64]. Yet, it was recently shown that ZBW and (G)AL can fail even qualitatively in some regimes of setups as simple as a DQD coupled in parallel to a single SC lead [35]. An alternative method that allows one to overcome these limitations is the recently introduced surrogate model [65– 67, which relies on exact diagonalization (ED) of SC-AIM with a discretized reservoir using only a small number of effective levels. The parameters of the approximate model are determined by minimizing a cost function that measures the difference between the surrogate and the exact tunneling self-energy.

Here, we present a conceptually different approach. We show that by directly employing a tight-binding chain representation of the hybridization function, one can construct optimal and scalable effective models for the low-energy physics of SC-AIM with arbitrary numbers of leads and QDs in a straightforward and systematic way. The idea of expanding the tunneling self-energy into a chain is not new. Exact unitary transformations that map a system coupled to a continuum onto a one-dimensional chain with only nearest-neighbor interactions have been derived for various models [68]. Similar mappings are widely used in methods such as NRG [40], the density matrix renormalization group (DMRG) [30], auxiliary quantum master equation approaches [69–71], and even machine learning techniques for extracting effective quantum impurity models [72, 73].

However, in this paper, we show that a properly constructed chain expansion (ChE) model naturally yields a Padé approximant of the original tunneling self-energy of the SC-AIM. Consequently, for many relevant problems and geometries, finite chains of only a few sites long are already sufficient to capture the effects of the SC leads. Moreover, the model parameters can be obtained explicitly and reduced to simple analytic formulas in both the wide-band and infinite-chain limits. To complement the paper, we provide a Jupyter notebook [74] with examples illustrating how the ChE models introduced here can be applied to different system geometries. It is worth noting that $Pad\acute{e}$ approximants are also widely used in other contexts related to impurity problems, for example, as analytical continuation methods [75–78] and to decompose the bath's Fermi function [79–81].

We first demonstrate the advantages of the ChE approach by revisiting selected problems that were previously studied using other methods, both in and out of equilibrium. We then focus on SC systems with multiple QDs arranged in parallel with respect to the SC lead. We show that small ChE models can be efficiently solved using ED, while longer chains, when needed, can be treated using DMRG. We also discuss how the method can be incorporated into other equilibrium and non-equilibrium techniques. This allows for the construction of fast, reliable, and systematically improvable effective models that are well-suited for a broad range of problems in both theoretical and experimental contexts.

The remainder of the paper is structured as follows. In section II, we first introduce the SC-AIM in its general form (Sec. IIA). Then we construct its low-energy effective models using the ChE approach and derive their parameters (Sec. IIB), with further technical details provided in Appendices A and B. Section III illustrates both the strengths and limitations of the ChE models by reexamining systems and problems previously addressed using accurate numerical methods and alternative effective models. It also outlines general strategies for applying ChE models to various types of systems in several physical regimes. Section IV begins with an analysis of a DQD in a parallel configuration (Sec. IV A), focusing on the emergence of the triplet state and competing singlet phases. We then extend the analysis to the ground-state properties of triple and quadruple QD systems (Sec. IVB). The paper concludes with a summary of the main findings (Sec. V). Certain technical details are deferred to the Appendices A-D.

II. MODELS AND METHODS

A. Superconducting Anderson impurity model with multiple impurities

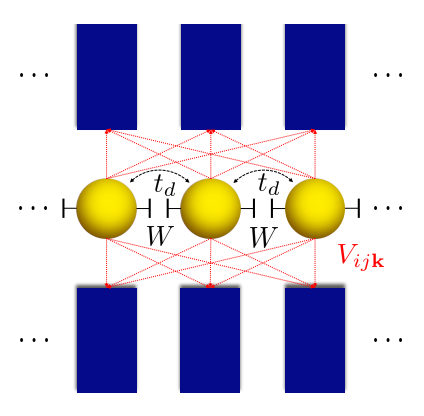


Figure 1. Illustration of N_d QDs coupled to N_l SC leads. Here, only nearest neighbor QDs interact with each other through hopping t_d and capacitance coupling W. Dots' interactions with leads are described by parameters V_{ijk} .

We consider a general model of interacting QDs that are coupled to SC reservoirs treated within the BCS theory (Fig. 1). Hamiltonian of such a hybrid structure with N_d QDs and N_l SC leads consists of three parts,

$$\mathcal{H} = \mathcal{H}^{\text{en}} + \sum_{l=1}^{N_l} \mathcal{H}_l^{\text{le}} + \sum_{j=1}^{N_d} \sum_{l=1}^{N_l} \mathcal{H}_{jl}^{\text{hy}}.$$
 (1)

The first part describes an ensemble of N_d interacting QDs,

$$\mathcal{H}^{\text{en}} = \sum_{j=1}^{N_d} \sum_{\sigma} \epsilon_j n_{j\sigma} + \sum_{j=1}^{N_d} U_j n_{j\uparrow} n_{j\downarrow}$$

$$- \sum_{i=1}^{N_d} \sum_{j=1}^{N_d} \sum_{\sigma} t_{ij} d_{i\sigma}^{\dagger} d_{j\sigma}$$

$$+ \sum_{i=1}^{N_d-1} \sum_{j>i}^{N_d} W_{ij} \left(n_{i\uparrow} + n_{i\downarrow} \right) \left(n_{j\uparrow} + n_{j\downarrow} \right),$$

$$(2)$$

where $d_{j\sigma}^{\dagger}$ $(d_{j\sigma})$ creates (annihilates) an electron with spin σ on the impurity j with energy ϵ_j and $n_{j\sigma} = d_{j\sigma}^{\dagger} d_{j\sigma}$. The second term stands for the local Coulomb interaction with strength (charging energy) U_j on the dot j. The third term describes direct hopping between the dots with $t_{jj} = 0$ for all j, and the last term describes the inter-dot capacitive coupling. Matrix elements t_{ij}

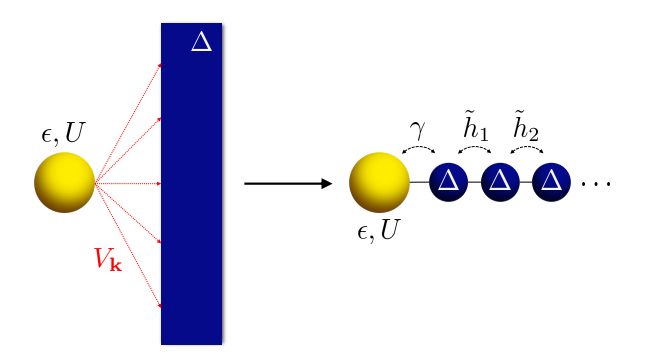


Figure 2. Mapping of an SC lead onto a finite tight-binding chain with site-dependent hopping amplitudes \tilde{h}_{ℓ} and local SC pairing. In the derivation of the ChE models, it is convenient to introduce the substitutions $\gamma = \sqrt{\Gamma \Delta h_0}$ and $\tilde{h}_{\ell} = \sqrt{h_{\ell}} \Delta$ with dimensionless coefficients h_{ℓ} .

and W_{ij} encode the geometry of the ensemble. For simplicity, in the following, whenever applied, we assume only nearest-neighbor hopping and capacitive coupling, with equal hopping amplitude t_d and coupling W for all connections. For convenience, we present results using shifted energy levels $\varepsilon_j = \epsilon_j + U_j/2 + \sum_{i \neq j} W_{ji}$ such that $\varepsilon_j = 0$ corresponds to the half-filled case on a bipartite lattice.

The second part represents N_l SC leads, each described by a standard BCS Hamiltonian,

$$\mathcal{H}_{l}^{\text{le}} = \sum_{\mathbf{k}\sigma} \epsilon_{l\mathbf{k}} c_{l\mathbf{k}\sigma}^{\dagger} c_{l\mathbf{k}\sigma} - \Delta \sum_{\mathbf{k}} \left(e^{i\varphi_{l}} c_{l\mathbf{k}\uparrow}^{\dagger} c_{l,-\mathbf{k}\downarrow}^{\dagger} + \text{H.c.} \right),$$
(3)

where $c_{l\mathbf{k}\sigma}^{\dagger}$ ($c_{l\mathbf{k}\sigma}$) creates (annihilates) an electron in lead l with spin σ and energy $\epsilon_{l\mathbf{k}}$, Δ is the SC gap and φ_l is the SC phase of lead l. We assume that all leads are made from the same material, as is common in experiments, and we use Δ as the energy unit within the paper and natural units for Planck constant $\hbar=1$ and elementary charge e=1.

The third part is the hybridization between the QD ensemble and the SC leads, which reads

$$\mathcal{H}_{jl}^{\text{hy}} = \sum_{\mathbf{k}\sigma} \left(V_{jl\mathbf{k}} c_{l\mathbf{k}\sigma}^{\dagger} d_{j\sigma} + \text{H.c.} \right). \tag{4}$$

The coupling to the leads is characterized by the tunneling rate matrix $\Gamma_{ij,l}(\epsilon) = \pi \sum_{\mathbf{k}} V_{il\mathbf{k}} V_{jl\mathbf{k}} \delta(\epsilon - \epsilon_{l\mathbf{k}})$, where the cross terms $i \neq j$ arise if multiple QDs are coupled to the same lead l. We assume a flat density of states with half-bandwidth D, $\rho(\epsilon) = \Theta(D - |\epsilon|)/(2D)$ and real $V_{il\mathbf{k}}$ which leads to $\Gamma_{ij,l}(\epsilon) = \Gamma_{ij,l}\Theta(|D - \epsilon|)$ with constant tunneling rates $\Gamma_{ij,l}$. In the paper, we use the convention of omitting subscripts to parameters whenever the same magnitude is assumed for all dots or leads.

B. Chain expansion and effective models

We demonstrate how to systematically construct increasingly accurate low-energy effective models using ChE of the tunneling self-energy. To illustrate the central idea, it suffices to consider the simplest case of a single QD coupled to a single lead, starting with the noninteracting limit U=0.

To avoid the complex analytic structure of real-frequency Green's functions, we adopt the Matsubara (imaginary-frequency) formalism. This eliminates the need to treat the behavior inside and outside the superconducting gap separately. Employing the Nambu spinor notation $\mathcal{D}^{\dagger} = (d_{\uparrow}^{\dagger}, d_{\downarrow})$ the impurity (QD) Green's function becomes [27]:

$$G_{0}(i\omega_{n})^{-1} = \begin{pmatrix} i\omega_{n} \left[1 + \frac{\Gamma}{\Delta} \widetilde{\Gamma}(\omega_{n}; D) \right] - \epsilon, & \Gamma \widetilde{\Gamma}(\omega_{n}; D) \\ \Gamma \widetilde{\Gamma}(\omega_{n}; D) & i\omega_{n} \left[1 + \frac{\Gamma}{\Delta} \widetilde{\Gamma}(\omega_{n}; D) \right] + \epsilon \end{pmatrix}.$$
(5)

Here, $\omega_n = (2n+1)\pi k_B T$ denotes the *n*th fermionic Matsubara frequency at temperature T, and the dimensionless hybridization function $\widetilde{\Gamma}(\omega_n; D)$ is given by

$$\widetilde{\Gamma}(\omega_n; D) = \frac{1}{\sqrt{1 + \frac{\omega_n^2}{\Delta^2}}} \frac{2}{\pi} \arctan \left[\frac{D/\Delta}{\sqrt{1 + \frac{\omega_n^2}{\Delta^2}}} \right]$$
 (6)

and

$$\widetilde{\Gamma}(\omega_n) \equiv \widetilde{\Gamma}(\omega_n; D \to \infty) = \frac{1}{\sqrt{1 + \frac{\omega_n^2}{\Delta^2}}},$$
 (7)

with Eq. (7) corresponding to the wide band limit (WBL). In what follows, we consider ω_n to be a continuous variable, consistent with the limit of T=0. The hybridization function plays a central role in our approach. We show next that due to the structure of Eq. (5), the additive nature of the tunneling self-energy, and the form of ChE, we are actually seeking the best approximations of Eq. (6) or Eq. (7), respectively.

Our main aim is to describe low-energy phenomena such as quantum phase transitions (QPTs), Andreev bound states, Josephson current (supercurrent), and related quantities in QD assemblies. Accordingly, our objective is to construct accurate, effective models in this regime. However, we are also interested in time-dependent phenomena, which may require an alternative effective model. Nevertheless, in both cases, we approximate the continuum bath with a finite chain of the same form. Among various chain configurations tested, the simplest and most effective is described by the Hamilto-

nian

$$\mathcal{H}_{U=0}^{\text{ChE}} = \sum_{\sigma} \epsilon_{\sigma} d_{\sigma}^{\dagger} d_{\sigma} - \sum_{\sigma} \left(\gamma d_{\sigma}^{\dagger} c_{1\sigma} + \text{H.c.} \right)$$
$$- \sum_{\ell=1}^{L-1} \sum_{\sigma} \left(\widetilde{h}_{\ell} c_{\ell\sigma}^{\dagger} c_{\ell+1,\sigma} + \text{H.c.} \right)$$
$$- \sum_{\ell=1}^{L} \left(\widetilde{\Delta} c_{\ell\uparrow}^{\dagger} c_{\ell\downarrow}^{\dagger} + \text{H.c.} \right),$$
(8)

where the lead is modeled by a tight-binding chain with L sites, as shown in Fig. 2. Here, γ is the hopping between the dot and the first site of the chain, \tilde{h}_{ℓ} are the inter-site hopping amplitudes, and $\tilde{\Delta}$ is the local SC pairing.

Using again the Nambu spinor notation $\mathscr{D}_{\mathrm{ChE}}^{\dagger}=(d_{\uparrow}^{\dagger},d_{\downarrow},c_{1\uparrow}^{\dagger},c_{1\downarrow},c_{2\uparrow}^{\dagger},c_{2\downarrow},\ldots,c_{L\uparrow}^{\dagger},c_{L\downarrow})$ we can write the noninteracting Green's function as

$$G_{U=0}^{\text{ChE}}(i\omega_{n})^{-1} = \begin{pmatrix} i\omega_{n} - \epsilon & 0 & \gamma & 0 & 0 & 0 & \cdots & 0 & 0 \\ 0 & i\omega_{n} + \epsilon & 0 & -\gamma & 0 & 0 & \cdots & 0 & 0 \\ \gamma & 0 & i\omega_{n} & \widetilde{\Delta} & \widetilde{h}_{1} & 0 & \cdots & 0 & 0 \\ 0 & -\gamma & \widetilde{\Delta} & i\omega_{n} & 0 & -\widetilde{h}_{1} & \cdots & 0 & 0 \\ 0 & 0 & \widetilde{h}_{1} & 0 & i\omega_{n} & \widetilde{\Delta} & \cdots & 0 & 0 \\ 0 & 0 & 0 & -\widetilde{h}_{1} & \widetilde{\Delta} & i\omega_{n} & \cdots & 0 & 0 \\ \vdots & \vdots & \vdots & \vdots & \vdots & \vdots & \ddots & \vdots & \vdots \\ 0 & 0 & 0 & 0 & 0 & 0 & \cdots & i\omega_{n} & \widetilde{\Delta} \\ 0 & 0 & 0 & 0 & 0 & 0 & \cdots & \widetilde{\Delta} & i\omega_{n} \end{pmatrix}$$

It is also convenient to introduce rescaling

$$\gamma = \sqrt{\frac{\Gamma}{\Delta} h_0} \Delta, \qquad \widetilde{h}_{\ell} = \sqrt{h_{\ell}} \Delta, \tag{10}$$

with dimensionless coefficients h_{ℓ} and $\widetilde{\Delta} = \Delta$ (see Appendix A).

As shown in Appendix A, the resulting dot Green's function takes a form analogous to Eq. (5):

$$G_{d,U=0}^{\text{ChE}}(i\omega_n)^{-1} = \begin{pmatrix} i\omega_n \left[1 + \frac{\Gamma}{\Delta} \mathcal{P}_L(\omega_n) \right] - \epsilon & \Gamma \mathcal{P}_L(\omega_n) \\ \Gamma \mathcal{P}_L(\omega_n) & i\omega_n \left[1 + \frac{\Gamma}{\Delta} \mathcal{P}_L(\omega_n) \right] + \epsilon \end{pmatrix},$$
(11)

where $\mathcal{P}_L(\omega_n; \{h_\ell\})$ is a rational function, with the form:

$$\mathcal{P}_L(\omega_n; \{h_\ell\}) = \frac{\sum_{j=0}^{L/2-1} p_j \omega_n^{2j}}{\sum_{j=0}^{L/2} q_j \omega_n^{2j}},$$
 (12)

for even L and

$$\mathcal{P}_L(\omega_n; \{h_\ell\}) = \frac{1}{1 + \omega_n^2} \frac{\sum_{j=0}^{(L-1)/2} p_j \omega_n^{2j}}{\sum_{j=0}^{(L-1)/2} q_j \omega_n^{2j}}, \quad (13)$$

for odd L. The coefficients p_i and q_i are functions of h_ℓ and follow directly from Eq. (A7).

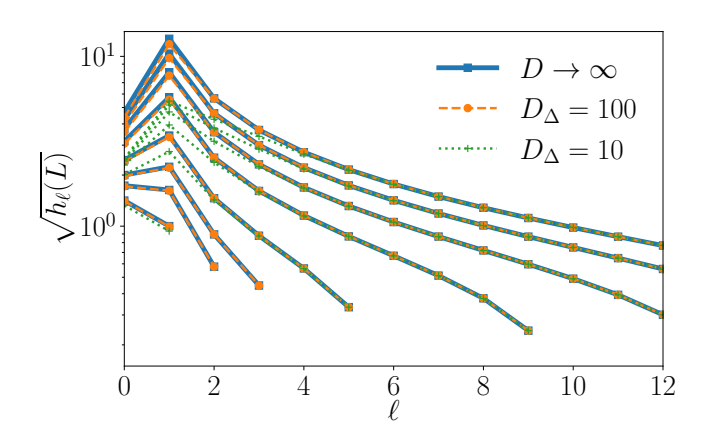


Figure 3. Square roots of first thirteen coefficients h_ℓ for ChE models with chain lengths ranging for (from left to right) L=2, 3, 4, 6, 10, 14, 20, and 22. Blue squares represent the ChE(L) model in WBL, orange circles correspond to ChE(L, $D_{\Delta}=100$), and green crosses to ChE(L, $D_{\Delta}=10$). Lines are included as guides to the eye. Note that we plot $\sqrt{h_\ell}$ as this is proportional to the hopping terms in the chain. Coefficients for $\ell>12$ are practically aligned for all three cases.

Here, the crucial observation is that Eq. (12) is of the same form as the $Pad\acute{e}$ approximant [82] $[L-2/L]_{\widetilde{\Gamma}(\omega_n)}(\omega_n)$ of the total hybridization function $\widetilde{\Gamma}(\omega_n;D)$ from Eq. (6) and that the second ratio in Eq. (13) has the form of the scaled $Pad\acute{e}$ approximant $[L-2/L-2]_{(1+\omega_n^2)\widetilde{\Gamma}(\omega_n)}(\omega_n)$. Therefore, to obtain $\mathcal{P}_L(\omega_n) \approx \widetilde{\Gamma}(\omega_n;D)$ around $\omega_n^2 = 0$ to order 2L-2, one simply needs to find coefficients h_ℓ that reproduce the respective $Pad\acute{e}$ coefficients. This is convenient as $Pad\acute{e}$ approximant of function f(x) is a rational fraction $[n/m]_f(x)$ (a degree-n polynomial in the numerator over a degree-m polynomial in the denominator) whose Maclaurin series matches that of f(x) up to order n+m. However, its radius of convergence can be much larger than that of the Maclaurin series.

The coefficients h_{ℓ} can be obtained by directly solving the system of equations for all independent parameters in the $Pad\acute{e}$ approximant. However, a more convenient approach is to use well-known continued fraction identities [83], which provide the h_{ℓ} coefficients directly. We outline this straightforward procedure in Appendix A, which includes illustrative examples, and also provide a Jupyter notebook with the implemented algorithm [74].

Given the popularity of the ZBW approximation and the practical relevance of the extended ZBW (eZBW) [35] – which correspond to ChE with L=1 and L=2, respectively – we record the closed-form coefficients below. Unlike typical ZBW/eZBW implementations, where parameters are phenomenologically fitted or tuned to a specific target, the ChE construction fixes them. For L=1

$$h_0 = \frac{2}{\pi} \arctan\left(D_\Delta\right) \tag{14}$$

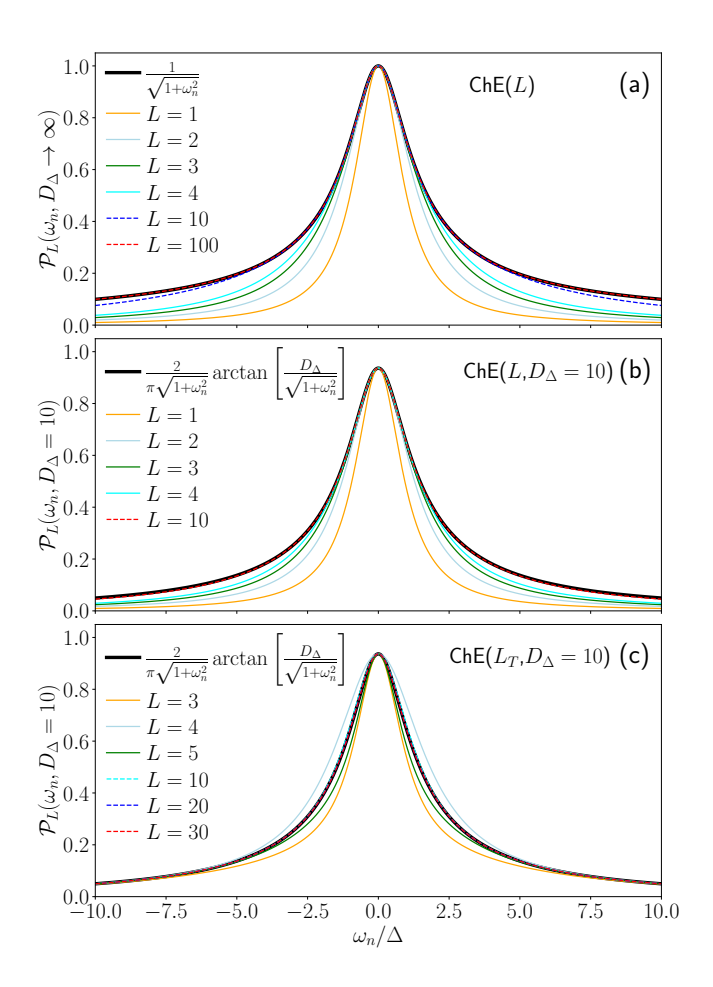


Figure 4. Comparison of the approximate function $\mathcal{P}_L(\omega_n,h_\ell)$ with the full hybridization function $\widetilde{\Gamma}(\omega_n;D)$ for $\Delta=1$. (a) WBL, where the coefficients h_ℓ take a simple analytic form (17). (b) Finite-bandwidth case with $D_\Delta=10$, where h_ℓ are obtained using the method described in the main text and Appendix A, based on matching the $Pad\acute{e}$ approximant to the full tunneling self-energy. (c) Truncated expansion of the infinite-chain model, where the last coefficient is evaluated using Eq. (A29), with $D_\Delta=10$. See also Fig. 30.

and L=2 case,

$$h_0 = \frac{2}{\pi} f(D_\Delta) \arctan(D_\Delta),$$

$$h_1 = f(D_\Delta) - 1,$$
(15)

where

$$f(D_{\Delta}) = 2 \frac{(1 + D_{\Delta}^2) \arctan(D_{\Delta})}{D_{\Delta} + (1 + D_{\Delta}^2) \arctan(D_{\Delta})}$$
(16)

with normalized half-bandwidth $D_{\Delta} = D/\Delta$.

Fortunately, in WBL $(D \to \infty)$, the coefficients h_{ℓ} take a simple form of rational numbers:

$$h_0 = L, \qquad h_{\ell>0} = \frac{L^2 - \ell^2}{4\ell^2 - 1}.$$
 (17)

For large but finite $D \gg \Delta$, the finite bandwidth introduces only small corrections to the coefficients h_{ℓ} , as

illustrated in Fig. 3. Consequently, the effective models constructed using the above coefficients are sufficient for most realistic systems where D is usually the largest energy scale. Therefore, most of the new results presented here are based on these simpler expressions.

However, finite-bandwidth corrections offer some distinct advantages. The finite-D approximation converges more rapidly to the exact hybridization function with increasing L than in the WBL [compare Figs. 4(a) and (b)]. Moreover, unlike the WBL expression, the finite-D coefficients do not diverge with L. The drawback of using finite D is that the calculation of the coefficients h_ℓ for $L\gtrsim 20$ becomes computationally demanding when arbitrary-precision arithmetic is employed, or numerically unstable otherwise, due to the appearance of large numbers in the $Pad\acute{e}$ approximant. This is not a problem for most ground-state investigations, where a typical system requires only a few sites in the chain, but it prohibits investigation of non-equilibrium phenomena where long chains are required.

However, there is a simple remedy for that. As demonstrated in Appendix A, a straightforward continued-fraction expansion of Eq. (6) can be used to derive the exact form of h_{ℓ} in the limit $L \to \infty$,

$$h_0 = \frac{2}{\pi} D_{\Delta}, \qquad h_{\ell>0} = \frac{\ell^2 D_{\Delta}^2}{4\ell^2 - 1}.$$
 (18)

Although not ideal for short-chain effective models, this form is useful when long chains are needed. It is particularly convenient when D_{Δ} is not too large (best if $D_{\Delta} < 20$). As a general strategy for the investigation of the non-equilibrium phenomena, we use both Eq. (17) and Eq. (18) to test the convergence. Both have their advantages and limitations as discussed in Sec. III, but give the same result for long enough chains and large enough D_{Δ} . When using Eq. (18), it is also convenient to truncate the chain by changing h_{L-1} to the value calculated using Eq. (A29), which significantly improves the low-energy behavior of shorter chains.

To distinguish between the methods using different expansion coefficients, we adopt the following notation: $\mathrm{ChE}(L)$ refers to models with coefficients h_ℓ given by Eq. (17), corresponding to WBL with L sites in the chain; $\mathrm{ChE}(L,D_\Delta)$ denotes models with coefficients h_ℓ derived for a finite bandwidth D_Δ and L sites in the chain; and $\mathrm{ChE}(L_T,D_\Delta)$ represents models where the coefficients h_ℓ are taken from the $L\to\infty$ solution in Eq.(18), but truncated via Eq. (A29) to include only the first L terms. The notation with L_∞ means that although the results are calculated with finite L, the correction of Eq. (A29) was not used to change the last h_{L-1} .

Figure 4 shows how the various expansions approximate the tunneling self-energy in the vicinity of $\omega=0$ on the imaginary-frequency axis. Together with its counterpart in Fig. 30 in Appendix A, it reveals that the ChE(L) and ChE(L, D_{Δ}) schemes are deliberately tailored to be optimal at $\omega_n=0$, and that their accuracy systematically extends to a wider imaginary frequency

window as L grows. Nevertheless, both schemes become inaccurate in the high-frequency limit, $|\omega_n| \to \infty$. By contrast, the ChE(L_T , D_{Δ}) expansion reproduces the high-frequency tails correctly even for short chains, yet a substantially larger number of sites is needed to capture the low-frequency regime around $\omega_n = 0$, particularly for large bandwidths [see Fig. 4(c) and Fig. 30(c) in Appendix A].

The generalization of ChE models to several dots and/or leads is straightforward. When a quantum dot j is coupled to multiple leads indexed by l, a separate chain can be introduced for each lead, characterized by its own hybridization Γ_{jl} , bandwidth D, superconducting order parameter $\tilde{\Delta}_l = \Delta_l e^{i\varphi_l}$, and length L. However, if several leads made of the same material (i.e., with identical D and Δ) are connected only to the same QD, they can be combined into a single effective chain (sChE). This mapping employs the geometric factor χ introduced in Ref. [38], along with minor adjustments of the chain parameters, as discussed in detail in Appendix B.

The situation is more involved when several dots are connected to the same lead. Consider, for instance, two dots (j = 1, 2) coupled to a common SC reservoir. The non-interacting Green's function, discussed in Appendix C, then contains non-local terms such as $V_{1l\mathbf{k}}V_{2l\mathbf{k}}$, which encode, among other things, the spatial separation of the impurities. Assuming real $V_{il\mathbf{k}}$, these mixed contributions can again be approximated by energy-independent tunneling rates $\Gamma_{jj',l}$. This is, however, a significant simplification; the actual dependence can be much more complex even in an isotropic environment [84].

By the Cauchy-Schwarz inequality, one may then write $\Gamma_{jj',l} = \zeta \sqrt{\Gamma_{j,l}\Gamma_{j',l}}$ with $\zeta \in \langle 0,1 \rangle$, which quantifies the correlations between the dots mediated by the shared lead. The most correlated case $\zeta = 1$ requires only a single effective channel, whereas generic ζ values necessitate two. Within the ChE framework we therefore connect both dots to two identical chains (l = 1, 2) with tunneling rates chosen as $\Gamma_{1,1} = (1 - \delta)\Gamma_1$, $\Gamma_{12} = \delta\Gamma_1$, $\Gamma_{21} = \delta\Gamma_2$, and $\Gamma_{22} = (1 - \delta)\Gamma_2$, where $\delta \in \langle 0, 0.5 \rangle$ and $\zeta = 2\sqrt{\delta(1-\delta)}$. The limit $\zeta = 0$ ($\delta = 0$) represents two dots that are not correlated through the substrate and thus effectively couple to independent reservoirs, whereas $\zeta = 1$ ($\delta = 0.5$) corresponds to a local two-level impurity coupled to a single SC bath. The ChE construction for systems with more than two dots follows by straightforward generalization. Some systems not treated in this work require a more careful application of the chain-expansion scheme. An example is a QD Aharonov–Bohm interferometer, where the two leads are directly hybridized [85].

Throughout this work, we adopt the standard gauge convention [27], which shifts the SC phases from the chain sites into the hybridization rates. This transformation leads to $\gamma_{jl} = \sqrt{h_0 \Delta \Gamma_{jl}} e^{i\varphi_l/2}$, while keeping the SC pairing term $\widetilde{\Delta} = \Delta$ and all other chain parameters real. The current operator J_{jl} , describing the particle

current between dot j and lead l within the ChE framework, can be derived directly from the time evolution of the particle number operator associated with the lead

$$J_{jl} = -\frac{dN_l}{dt} = i \left[N_l, \mathcal{H}^{\text{ChE}(L)} \right],$$

where the relevant part is given by the commutator with the dot-lead coupling term:

$$J_{jl} = -i \sum_{\sigma} \left(\gamma^* c_{1l\sigma}^{\dagger} d_{j\sigma} - \gamma d_{j\sigma}^{\dagger} c_{1l\sigma} \right). \tag{19}$$

Before presenting our results, we emphasize that the ChE framework is quite general and naturally encompasses several approaches previously employed in the literature. For example, the widely used ZBW method is equivalent to ChE with L=1, although the ZBW parameters are usually chosen arbitrarily. Our analysis reveals that $\mathrm{ChE}(L=1)$ fails to approximate the tunneling self-energy even at leading order in ω_n . In light of this, it is perhaps unsurprising that the ZBW method can yield qualitatively incorrect results, as recently demonstrated by Zalom et al. [35]. This observation is particularly significant given that ZBW is frequently used not only for qualitative understanding but also in the interpretation of experimental data.

In contrast, the slightly more sophisticated ChE(L =2), which corresponds to the eZBW method [35], often resolves these shortcomings. Unlike earlier eZBW implementations, our formulation fixes the coefficients in the low-energy expansion exactly, yielding a consistent and systematically controlled approximation. The surrogate models proposed by Baran et al. [65], although formulated differently, can likewise be interpreted as particular instances of the ChE framework. In their approach, the discretized reservoir parameters are adjusted to reproduce the tunneling self-energy across the full bandwidth for finite D, though the fitting procedure is intrinsically weighted toward low frequencies. However, to gain more insight into the surrogate-model eigen-states, the chain representation of discretized lead is also employed [65]. In this sense, their construction resembles $ChE(L_T, D_{\Lambda})$, whereas in our approach, the coefficients are provided analytically.

III. BENCHMARKING, USAGE STRATEGIES, AND ANCILLARY RESULTS

To illustrate both the strengths and limitations of effective ChE models, we reexamine a set of systems and problems that have previously been studied in the literature using precise methods and other effective models. Accordingly, we do not dwell on detailed recapitulations of established results. We instead concentrate on introducing some general strategies for employing ChE for

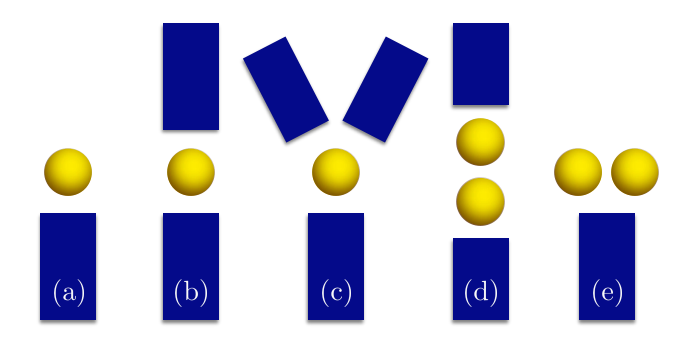


Figure 5. Illustration of systems used to benchmark the ChE models against previous results. (a) Single QD coupled to one lead. (b) Junction bridged by a QD. (c) Single QD coupled to three leads. (d) DQD in serial configuration. (e) DQD in parallel configuration.

different types of problems and testing its various versions. In this respect, the section also contains new ancillary results. For ground-state properties, we focus on setups that are amenable to accurate solutions via NRG. For time-dependent dynamics, we compare our results to those obtained using non-equilibrium Green's function (NEGF) techniques and briefly discuss the relation to other methods. To show the versatility of the ChE scheme, we address several system geometries illustrated in Fig. 5.

A. Single QD coupled to one SC lead

The equilibrium properties of a single QD coupled to one SC lead [Fig. 5(a)] can be efficiently addressed even by computationally demanding methods such as NRG and CT-HYB quantum Monte Carlo. This makes it an ideal benchmark system for testing the validity and convergence of ChE-based effective models. Figure 6 shows the evolution of excited in-gap many-body states over three orders of magnitude in U, for fixed ratios of $\Gamma/U=2$ (left column) and $\Gamma/U=0.2$ (right column). The black circles indicate NRG data calculated for a half-bandwidth of $D=100\Delta$. Consequently, results in the upper range correspond to values of U and Γ comparable to D, placing the system effectively in a small-gap regime where our approximations, relying on the SC character of the leads, are expected to break down.

We test three variants of ChE: the infinite-band approximation ChE(L) in (a1) and (a2); finite-band models $ChE(L, D_{\Delta} = 100)$ in (b1) and (b2); and the truncated expansion $ChE(L_T, D_{\Delta} = 100)$ in (c1) and (c2). Panels (a1)-(b2) clearly demonstrate that both ChE(L) and $ChE(L, D_{\Delta})$ with two to four sites in the chain suffice to accurately reproduce the NRG results over more than two orders of magnitude in U/Δ . Furthermore, as L increases, the ChE models show systematic improvement

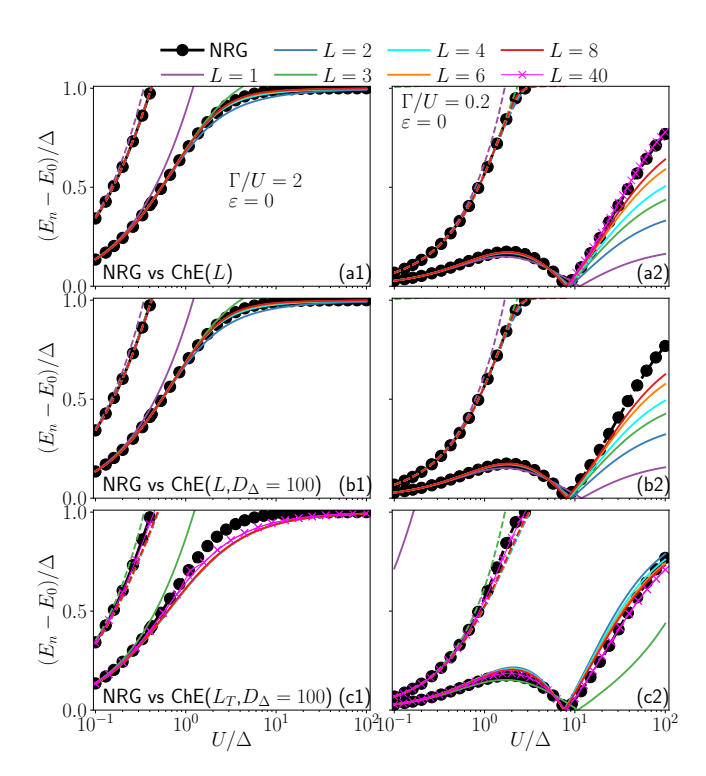


Figure 6. Single QD coupled to a single SC lead, as illustrated in Fig. 5(a). Comparison of the excited in-gap states calculated with various versions of ChE effective models to the NRG data over three orders of magnitude of U for fixed ratios $\Gamma/U=2$ (left column) and $\Gamma/U=0.2$ (right column). The NRG data (black circles) have been calculated for half-bandwidth $D=100\Delta$. Panels (a1) and (a2) show infinite band ChE(L), panels (b1) and (b2) the finite band ChE(L, $D_{\Delta}=100$), and panels (c1) and (c2) the truncated ChE(L_T , $D_{\Delta}=100$). All results are for the half-filled case $\varepsilon=\epsilon+U/2=0$.

even in the regime $U\gg \Delta$. We present results up to L=8, which can be readily solved via Lanczos ED within minutes on a standard PC. To illustrate convergence, we also include DMRG results for ChE with L=40 [purple crosses in panel (a2)], which are in very good agreement with NRG, despite the use of the infinite-D approximation in a regime where U is comparable with D.

Panels (c1) and (c2) show that, although the truncated expansion does not match the precision of $\mathrm{ChE}(L)$ at small L, it still yields robust effective models, particularly for small Γ/U , and its accuracy improves with increasing L. Nevertheless, the true usefulness of this approach will become apparent in problems that require long chains.

Figure 7 shows the phase diagram of the half-filled $(\varepsilon = \epsilon + U/2 = 0)$ SC-AIM, with the phase boundary separating the singlet and doublet ground states. The NRG results (black circles) are compared with GAL (purple dashed line) and ChE(L) for L=2, 6, and 8 (solid lines). Panels (a) and (b) present the same data on different scales to better emphasize the differences across regimes. Notably, even ChE(L=2) shows better agree-

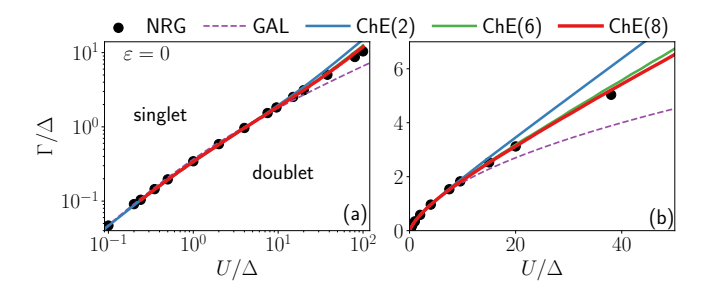


Figure 7. Single QD coupled to a single SC lead as illustrated in Fig. 5(a). Phase boundary between the singlet and doublet ground state at half-filling estimated from NRG (black circles), GAL (dashed purple line), and ChE(L) (solid lines) for different L. Panels (a) and (b) show the same results using different scales.

ment with NRG (being virtually exact for $U < 10\Delta$) than GAL. Moreover, increasing L extends this agreement to larger values of U/Δ .

However, it is important not to overstate these results. Although computationally trivial, ChE(L=2) still represents an interacting model with three sites. In contrast, the GAL result is based on a compact analytical formula [34, 60]:

$$\left(\frac{U}{2\left(1 + \frac{\Gamma_T}{\Delta}\right)}\right)^2 = \varepsilon^2 + \Gamma_T^2 \cos^2\left(\frac{\phi}{2}\right), \qquad (20)$$

shown here for the more general case of two equally coupled leads with $\Gamma_1 = \Gamma_2 = \Gamma_T/2$ and a Josephson phase $\varphi = \varphi_1 - \varphi_2$. For a single lead, we have $\varphi = 0$ and $\Gamma_T = \Gamma$, which further simplifies the expression. Despite its simplicity, GAL captures the phase boundary with experimental-level precision in the weak to intermediate interaction regime.

The true strength of the ChE approach, however, becomes evident away from half-filling, where GAL requires phenomenological corrections, and in more complex systems where GAL and other commonly used effective models may even fail qualitatively.

B. Single QD coupled to multiple SC leads

The system of two SC leads connected via QD [Fig. 5(b)] is of central importance. Depending on the parameter regime, it represents a generalized Josephson junction or an impurity on the SC surface probed by an SC STM tip. Moreover, it has recently been shown that any single-dot multiterminal system without direct inter-lead coupling can be exactly mapped to a QD symmetrically coupled to only two leads [38]. This is of particular importance, as three-terminal QD devices can be used to construct SC diodes and transistors, and even greater functionality is expected in more complex configurations. In addition, considerable effort has been

devoted to studying out-of-equilibrium phenomena, including current at finite voltages and the microwave response of such systems. These offer enhanced tunability and access to dynamical information via the supercurrent response. Consequently, there is significant value in developing effective models that enable fast and reliable parameter scans in equilibrium as well as to address long-time dynamics.

a. Equilibrium properties: The central quantity for the investigation of the junction is the supercurrent, which, for a finite Josephson phase φ , flows through the QD even in equilibrium. A sudden reversal of its direction upon tuning a parameter signals a QPT between singlet and doublet phase, i.e., crossing of the many-body ground state with the first excited state of different character.

In Fig. 8 we compare the NRG results for the supercurrent in a system with $\Gamma_1 = \Gamma_2 \equiv \Gamma = \Delta$ and three interaction strengths U = 2 (black), U = 4 (blue) and U = 8 (red circles) with the predictions of GAL (a), ChE(L = 2, 4) (b,c) and $ChE(L = 1, 2, 4, D_{\Delta} = 100)$ (d-f). As shown in panel (a) and discussed in detail in Ref. [34], for the geometry of Fig. 5(b), the GAL model yields a qualitatively incorrect Josephson current J as it vanishes in the doublet phase and is independent of U in the singlet phase. A band correction, denoted GAL+C in Ref. [64], is needed to tame these shortcomings. In contrast, ChE-based models do not suffer from these limitations because the band influence is encoded directly in the chain representation. Remarkably, even for L=1, equivalent to ZBW [Fig. 8(d)], $ChE(L = 1, D_{\Delta} = 100)$ already provides a reasonable estimate of J, and the agreement improves systematically with increasing L. Panels (b) and (c) further demonstrate that for short chains and large U, the simpler ChE(L), which uses analytical chain coefficients, can match $\mathrm{ChE}(L,D_\Delta)$, justifying its use for systems with sufficiently wide band.

Beyond the qualitative issues noted above, the GAL model is in good quantitative agreement with NRG only near half filling ($\varepsilon=0$). Therefore, a phenomenological scaling, leading to the MGAL model, was introduced in Refs. [34, 37]. The improvement is evident in Fig. 9(a), which shows the in-gap spectrum as a function of ε for Josephson phase $\varphi=0.9\pi$. The ChE(L) models, by contrast, require neither such corrections nor the ad-hoc parameter tuning often employed in ZBW studies. Shortchain models already reproduce the NRG results with high accuracy far from half-filling, as shown in Fig. 9(b).

To demonstrate the versatility of ChE models, we briefly discuss results for a three-terminal setup illustrated in Fig. 5(c). Figure 10 shows the supercurrent flowing between the QD and the second terminal for the system with $\Gamma_1 = 0.45\Delta$, $\Gamma_2 = 0.4\Delta$, $\Gamma_3 = 0.15\Delta$, $U = 3\Delta$, $\varepsilon = 0$, $\varphi_1 = 0$, and $\varphi_3 = 0$. The black circles show the NRG result (taken from Ref. [38]). These have been obtained by using the exact transformation introduced in Ref. [38]. This means that the raw data have

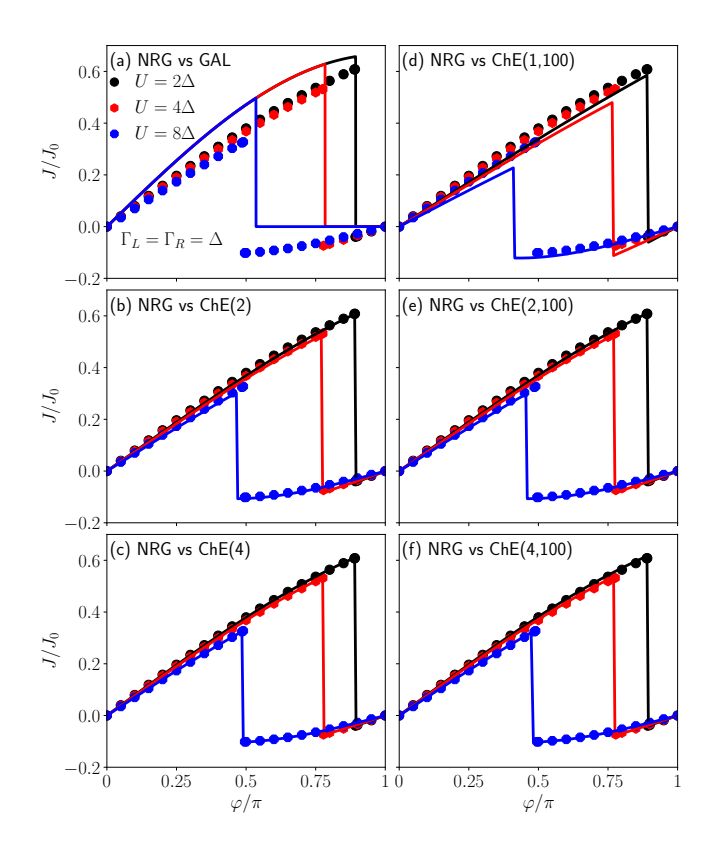


Figure 8. Single QD between two SC leads as illustrated in Fig. 5(b). Comparison of the supercurrent as a function of the Josephson phase for different U at half-filling ($\varepsilon=0$) between NRG (black circles) and GAL (a), infinite band $\mathrm{ChE}(L=2)$ (b), $\mathrm{ChE}(L=4)$ (c), finite band $\mathrm{ChE}(L=1,D_\Delta=100)$ (d), $\mathrm{ChE}(L=2,D_\Delta=100)$ (e), and $\mathrm{ChE}(L=4,D_\Delta=100)$ (f). The NRG data were calculated for $D=100\Delta$ and $J_0=e\Delta/\hbar$.

been obtained for a two-terminal setup and then mapped to three terminals. In contrast, the ChE results in panel (a) are a direct calculation, where each lead was approximated by its own short chain of two sites. The results are in very good agreement.

Using the geometric factor of Ref. [38] (see Appendix B), multiple leads attached to the same dot can be mapped to a single chain. As shown in panel (b), the sChE representation matches the accuracy of the direct multi-chain calculation while yielding a much smaller effective model.

For this setup and for the cases in Figs. 8–9, the direct construction is therefore unnecessary. Nevertheless, it remains useful when the single-chain reduction does not apply—for example, when leads couple to multiple different dots, when metallic and SC leads coexist, when the SC gaps differ in magnitude, or under non-equilibrium driving. The direct formulation also enables hybrid strategies, e.g., to treat selected channels with NRG while describing additional leads by short ChE chains.

b. Driven systems: ChE models are not confined to equilibrium situations. To illustrate their scope, we con-

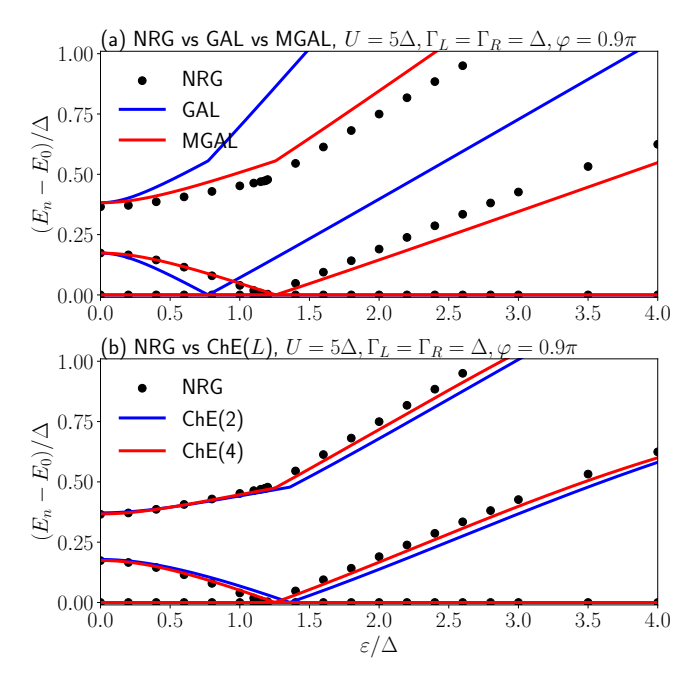


Figure 9. Evolution of the in-gap states away from half filling for a single QD between two SC leads as illustrated in Fig. 5(b). (a) Comparison between the NRG (black circles), GAL (blue lines), and MGAL (red lines) results. (b) Comparison of NRG data (black circles) with ChE(L=2) (blue lines) and ChE(L=4) (red lines).

sider here a junction subjected to a finite bias voltage.

Figure 11 displays the transient current of a non-interacting junction (U=0) that is quenched from zero bias (V=0) to a finite bias $V=0.8\Delta$, where $V=\mu_1-\mu_2$, i.e., the difference between the chemical potentials of the leads. We use $\Gamma=0.4\Delta$, $\varphi=0$, and $\varepsilon=0$ because the same protocol was analysed by Cheng et al. in Ref. [32] with Keldysh NEGF; the gray squares represent their data taken from Fig. 7 of Ref. [32].

To tackle the quench, we follow the unitary transformation of Ref. [32]. For the special case $\Gamma_1 = \Gamma_2$ and $\mu_1 = -\mu_2$, it transfers the static bias of the leads into time-dependent phases:

$$\mu_{1} = \frac{V}{2} \to \mu_{1} = 0, \qquad \mu_{2} = -\frac{V}{2} \to \mu_{2} = 0,$$

$$\varphi_{1} = \frac{\varphi}{2} \to \varphi_{1}(t) = \frac{\varphi}{2} + Vt,$$

$$\varphi_{2} = -\frac{\varphi}{2} \to \varphi_{2}(t) = -\frac{\varphi}{2} - Vt,$$
(21)

which leads to complex, time-dependent couplings $\gamma_l(t) = \sqrt{h_0 \Delta \Gamma_l} \, e^{i \varphi_l(t)/2}$. Because of U=0 ChE representation reduces to a tight-binding chain and, therefore, the evolution of chains comprising thousands of sites is straightforward, allowing us to examine relaxation processes over long time scales.

As Fig. 11(a) shows, a chain of only L=50 sites already reproduces the NEGF result up to the steady-state. Shorter chains, such as L=20, are inadequate

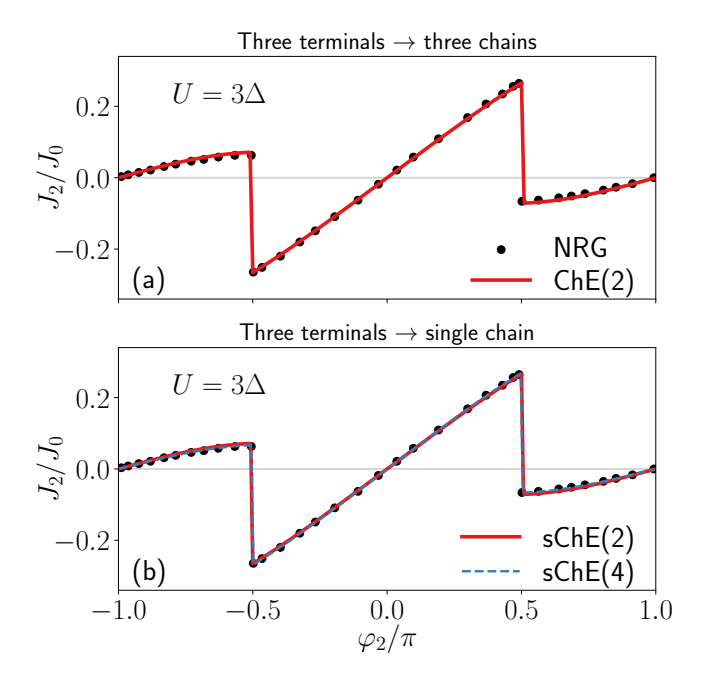


Figure 10. Supercurrent between the QD and the second lead in the three-terminal setup shown in Fig. 5(c) with $\Gamma_1=0.45\Delta$, $\Gamma_2=0.4\Delta$, $\Gamma_3=0.15\Delta$ and $\varphi_1=\varphi_3=0$. Black circles denote NRG data obtained for a two-terminal setup and mapped to the three-terminal case via the transformation of Ref. [38]. (a) Comparison with ChE(L=2) (red line) using three chains, each representing a single lead. (b) Comparison with sChE(L) using a single chain to model all three leads, as described in Appendix B: red solid line for L=2 and blue dashed line for L=4.

because the signal reflected at the end of the chain reaches the dot before relaxation is completed. In this respect, the infinite-band $\mathrm{ChE}(L)$ representation is superior to its truncated counterpart $\mathrm{ChE}(L_T,D_\Delta)$, shown in Fig. 11(b), which requires longer chains. This stems from the larger hopping amplitudes \tilde{h}_ℓ in the truncated model as the propagation time between neighboring sites scales as $1/\tilde{h}_\ell$. Hence, as Fig. 11(c) illustrates, if finite D_Δ is required, it is advantageous to employ the smallest bandwidth permitted by the physical problem.

Despite the need for longer chains when analyzing long-time dynamics, the truncated representation can still be preferable in certain contexts. $\mathrm{ChE}(L)$ possesses a distinct parameter set h_ℓ for every chain length, so short-time dynamics vary slightly with L even when the initial state is identical, giving rise to the small oscillations visible in panel (a) even for short times. By contrast, the coefficients up to the site L_T are identical for any chain length in $\mathrm{ChE}(L_T, D_\Delta)$, because they are derived from the $L \to \infty$ limit. Consequently, the dynamics coincide for different L until finite-size effects, namely the backpropagation of the signal reflected from the chain end, become relevant. In addition, spurious small oscillations are absent for $\mathrm{ChE}(L_T, D_\Delta)$.

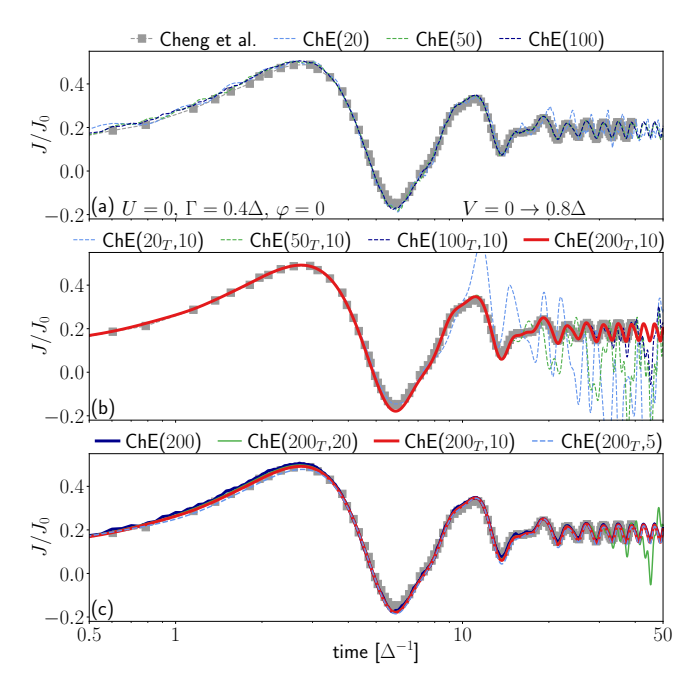


Figure 11. Single QD between two SC leads as illustrated in Fig. 5(b). Transient current after a quench from zero to a finite bias. Grey squares: data extracted from Cheng et al. [32], obtained with the NEGF approach. (a) Comparison with a tight-binding $\mathrm{ChE}(L)$ chain. (b) Results of $\mathrm{ChE}(L_T, D_\Delta = 10)$ for several Ls. (c) Influence of the bandwidth on the transient dynamics.

C. Junction with a double QD in serial configuration

Serial DQDs sandwiched between two SC leads have become an active field of study due to the potential to host qubits [24, 39, 86] and their advanced tunability because, in principle, the parameters of each dot, in particular the level energies ϵ_j , can be tuned independently [6, 7, 87-89]. This tunability was recently exploited in a proposal predicting an anomalous time-averaged Josephson current-phase relation, including complete rectification, when phase-shifted microwave gates are applied [90]. For the latter, the results were obtained in the $\Delta \to \infty$ atomic limit or for a noninteracting system $(U_1 = U_2 = 0)$, and it is therefore not clear how they translate to more realistic conditions. Nonetheless, it was already shown that, in equilibrium, (G)AL does not suffer from the qualitative drawbacks observed for a single-QD junction [34], suggesting that the nonequilibrium finite U predictions may also remain qualitatively valid.

1. Equilibrium properties

Although (M)GAL remains quantitatively reliable across a wide parameter range, it fails in the strong-

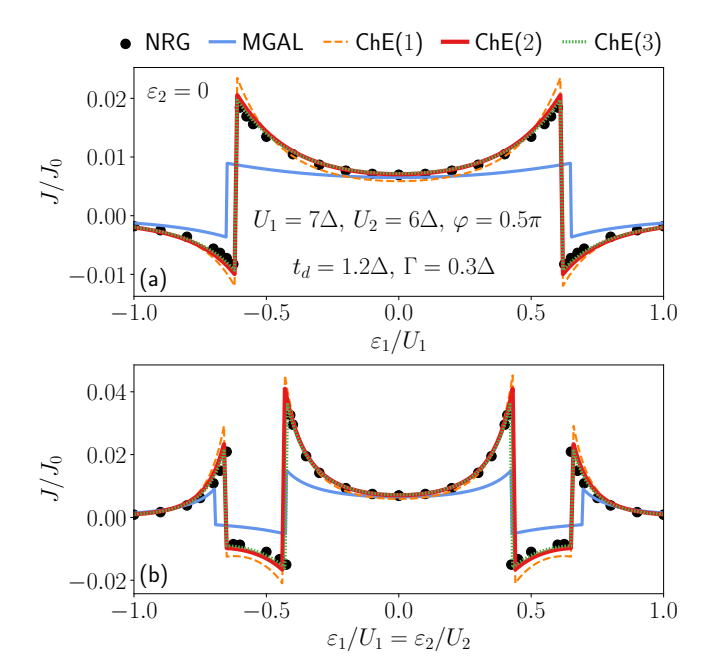


Figure 12. Serial DQD between two SC leads as illustrated in Fig. 5(d). Josephson current for the experimental parameters of Ref. [6] as a function of ε_1/U_1 with $\varepsilon_2 = 0$ (a) and for $\varepsilon_1/U_1 = \varepsilon_2/U_2$ (b). Black circles: NRG; blue line: MGAL [34]; orange, red, and green lines: ChE(L) for L = 1, 2 and 3, respectively. We use shifted energy levels $\varepsilon_j = \epsilon_j + U/2$.

interaction limit relevant to many experiments. Figure 12 probes this limit using the parameters of Ref. [6]: $U_1 = 7\Delta$, $U_2 = 6\Delta$, $t_d = 1.2\Delta$, $\Gamma = 0.3\Delta$, $\varphi = \pi/2$ and W = 0. Panel (a) displays the equilibrium Josephson current J versus ε_1/U_1 at fixed $\varepsilon_2 = 0$, whereas panel (b) follows J along $\varepsilon_1/U_1 = \varepsilon_2/U_2$. While MGAL (blue line) locates the singlet-doublet phase boundary, signaled by the sign reversal of J, its magnitude deviates markedly from the NRG results. In contrast, the ChE model already improves the agreement at L = 1 (dashed orange line) and converges rapidly to NRG as L increases.

2. Driven systems:

Figure 13 revisits the phase-shifted microwave drive analyzed by Ortega-Taberner *et al.* [90] (cf. Fig. 10 therein). The dot levels are modulated as

$$\varepsilon_1(t) = \varepsilon_0 + A\cos(\omega t), \quad \varepsilon_2(t) = \varepsilon_0 + A\cos(\omega t + \theta), \quad (22)$$

but, in contrast to the original study, we retain a finite SC gap and set $\Gamma=0.1\Delta$. Panel (a) shows the time-averaged Josephson current for U=0 and several values of L, demonstrating that finite-L effects are negligible in this regime as the lines lie practically on top of each other. This is because already ChE with L=1 gives a good estimate of the in-gap states. Panel (b) introduces a finite

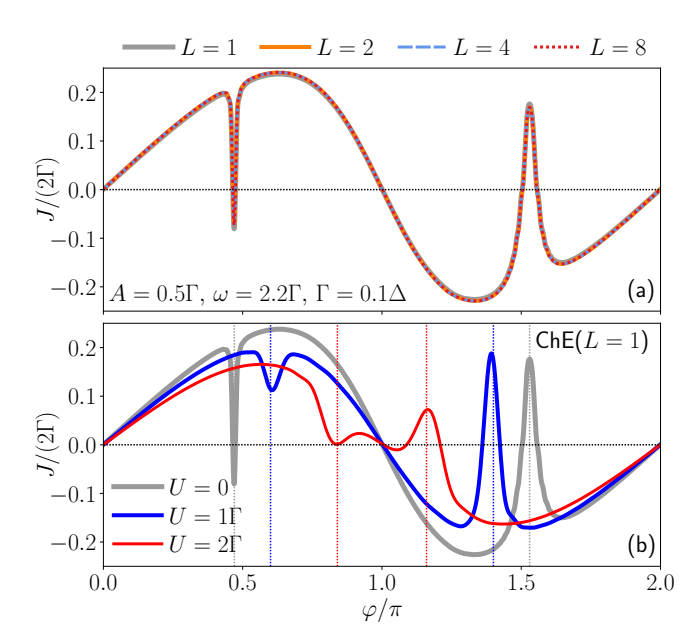


Figure 13. Serial DQD between two SC leads as illustrated in Fig. 5(d). Time-averaged Josephson current J as a function of the Josephson phase φ (current-phase relation). Parameters are taken from Ref. [90], except for Δ , which is set to unity. To allow for an easier comparison with Ref. [90], we plot the data in units of Γ . The microwave drive frequency is set to $\omega=2.2\Gamma$ with amplitude $A=0.1\Gamma$ and phase shift $\theta=0.5\pi$. (a) Non-interacting case with data obtained with $\mathrm{ChE}(L)$ for L=1,2,4, and 8. (b) Impact of a finite Coulomb interaction U. Because the curves are extracted from direct real-time evolution with the initial state being the singlet ground state, only resonances from the singlet sector are visible. Their depth may depend on numerical details such as the sampling frequency.

on-site interaction U. Vertical lines of the corresponding color mark Josephson phase φ where the singlet ingap states meet integer multiples of the drive frequency, thereby identifying the origin of the observed anomalies. Clearly, these resonances persist even for $U=0.2\Delta$, although their position shifts and their width grow with increasing U. Our data were obtained by unitary time evolution from the singlet ground state at $\varepsilon_{1,2}(t)=\varepsilon_0$, therefore we probe only singlet-sector resonances. Coupling the ChE model to an effective metallic bath or using a mixed state at t=0, could lift this restriction, but it is left for future work.

D. Double QD coupled to a common lead

As a final benchmark, we consider the parallel double-dot geometry sketched in Fig. 5(e). Recent NRG analysis by Zalom et al. [35] revealed a parameter window in which the ground state of this device is a triplet. Neither the ZBW model nor (G)AL can capture this regime, as both allow only singlet or doublet ground states. The

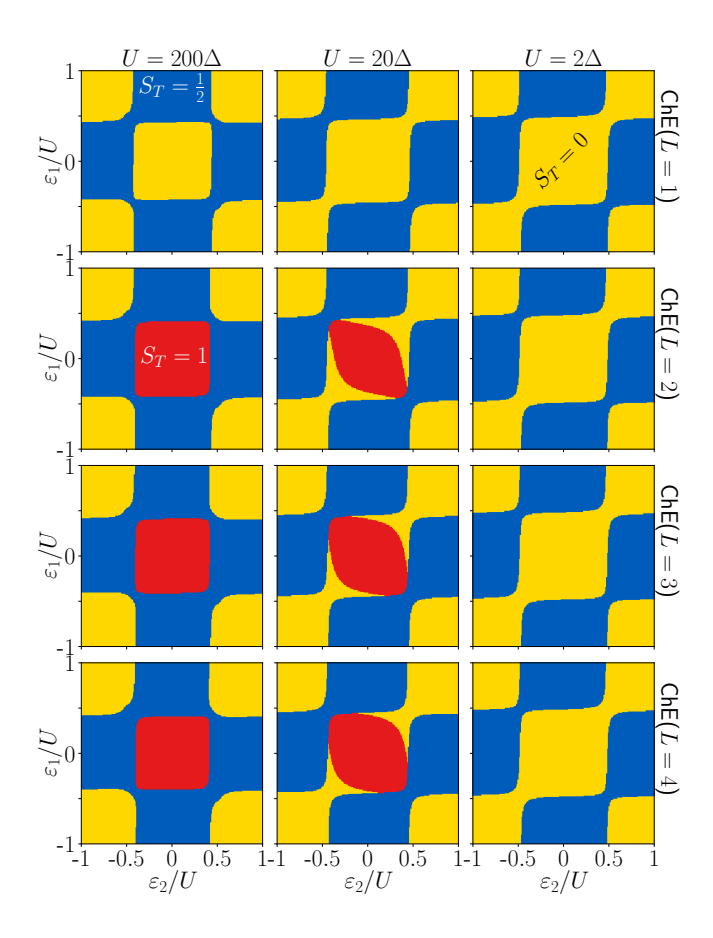


Figure 14. Phase diagrams away from half-filling for parallel DQD coupled to a single lead, illustrated in Fig. 5(e) for $U=200\Delta$ (left column), $U=20\Delta$ (center column), and $U=2\Delta$ (right column). Each color represents a different value of total spin, yellow for $S_T=0$, blue for $S_T=1/2$, and red for $S_T=1$. The model parameters $\Gamma=0.05U$, $t_d=0$ and W=0 are taken from Ref. [35]. First line shows results of ChE(L=1) (ZBW), second of L=2 (eZBW), third L=3 and forth L=4, showing fast convergence.

eZBW construction of Ref. [35] remedies the problem qualitatively. The ChE framework delivers the eZBW parameters directly and, when necessary, enables systematic improvements beyond eZBW. Figure 14 shows the result of ChE results for L=1,2,3,4 and parameters of Fig. 2(e), (g), (h) in Ref. [35]. The colors represent different values of the total spin of the system,

$$\hat{\mathbf{S}}_T^2 |\psi_{\rm GS}\rangle = \left(\sum_i \hat{\mathbf{S}}_i\right)^2 |\psi_{\rm GS}\rangle = S_T(S_T + 1) |\psi_{\rm GS}\rangle, \quad (23)$$

where i runs through all sites (QDs and chain sites) and $|\psi_{\rm GS}\rangle$ is the ground state. The yellow areas show singlet $(S_T=0)$, blue doublet $(S_T=1/2)$, and red triplet $(S_T=1)$ ground state. Qualitatively, we observe the same behavior as discussed in Ref. [35], that is, L=1 (ZBW) is too simple to capture the triplet ground state. The extension to L=2 (eZBW) is already sufficient to solve the problem. Note that despite the strong interac-

tions ($U=200\Delta$, 20Δ , 2Δ), ChE reproduces the NRG results with high fidelity. Although each panel in Fig. 14 consists of 221×221 points, the diagrams were produced by ED on a standard PC. Because the parallel-dot configuration remains comparatively unexplored, we return to its ground-state phase diagram in Sec. IV A.

IV. RESULTS: MULTIPLE QUANTUM DOTS COUPLED TO THE SAME SC LEAD

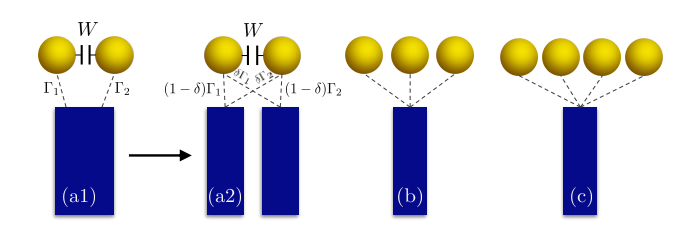


Figure 15. Illustration of the systems investigated in Sec. IV. (a) Double QD coupled to a single SC lead. For $\zeta \neq 1$ ($\delta \neq 0.5$), this system maps onto two coupled chains. (b) Triple and (c) quadruple QDs with identical dots and couplings in the maximally correlated case $\zeta = 1$.

We use the $\mathrm{ChE}(L)$ method supported by NRG data to investigate the ground state properties of multiple QDs coupled to the same lead, as illustrated in Fig. 15. We will first revisit the DQD from the previous section Sec. III D, as it is a rich system with several open problems. Then we will address the ground state of triple and quadruple dots.

A. Double QD

As briefly outlined in Sec. IIID and examined in detail in Ref. [35], a DQD in the parallel configuration with $\zeta=1$ already falls outside the reach of the most commonly employed effective descriptions, such as the ZBW and (G)AL. Extending the chain to larger L resolves this limitation, yet, as we show below, short chains may still be inadequate for quantitative work in parts of the regions where L=1 fails completely. To streamline the analysis, we first neglect both the direct inter-dot hopping t_d and the capacitance W and focus on the half-filled case.

Figure 16(a1) displays a color map of the total spin S_T in the $\Gamma - U$ plane, obtained with ChE(L=4) at half-filling. Yellow, blue, and red regions correspond to singlet, doublet, and triplet ground states, respectively.

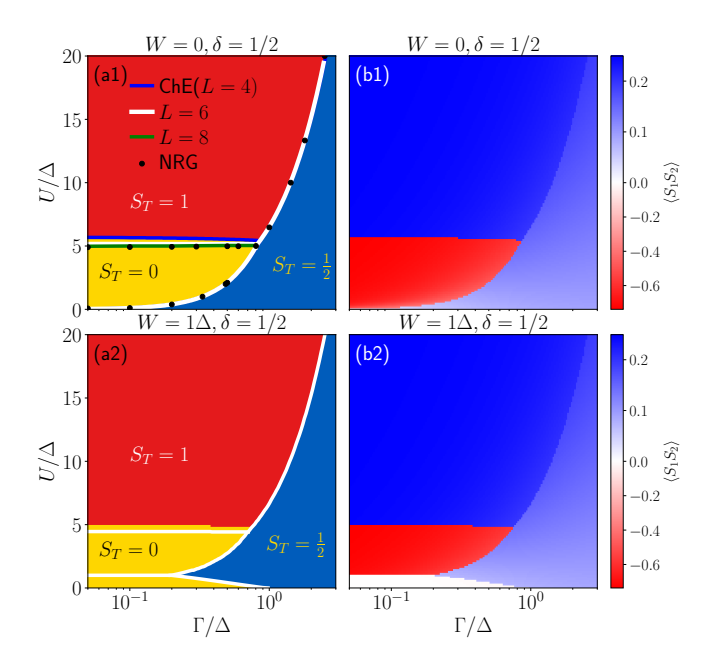


Figure 16. Phase diagrams for the DQD system sketched in Fig. 15(a1). (a1) Total spin S_T in the $\Gamma - U$ plane for symmetric dots, $\Gamma_1 = \Gamma_2 \equiv \Gamma$ and $U_1 = U_2 \equiv U$, at half-filling, W = 0, and in the maximally correlated limit $\zeta = 1$ ($\delta = 0.5$) calculated with ChE(L = 4). (b1) Corresponding average spin correlation $\langle \hat{\mathbf{S}}_1 \cdot \hat{\mathbf{S}}_2 \rangle$. (a2) Same as (a1) but with a finite inter-dot capacitive coupling $W = \Delta$. (b2) Mean spin correlation for the parameters of (a2). Phase boundaries (solid lines) computed with ChE(L = 4, 6, 8) and critical points (black circles) obtained with NRG were determined from the positions of the QPT in the in-gap spectrum. Maps have been obtained with ChE(L = 4).

Panel (a2) shows the expectation value of spin correlations $\langle \hat{\mathbf{S}}_1 \cdot \hat{\mathbf{S}}_2 \rangle$, i.e., effective exchange, revealing that the singlet region is stabilized by an effective antiferromagnetic exchange, while the triplet region exhibits a ferromagnetic one. As noted previously in different contexts [20, 91], the doublet state likewise entails an effective ferromagnetic coupling, whose strength grows with both Γ and U.

The colored lines in Fig. 16(a1) mark the phase boundaries obtained with $\mathrm{ChE}(L)$ for several chain lengths, and black circles denote the benchmark NRG results. The singlet-doublet and triplet-doublet boundaries converge rapidly with L, but the singlet-triplet line shifts appreciably toward lower U as L increases.

This slow convergence is highlighted in Fig. 17: panel (a) shows the in-gap excitation energies, panel (b) the induced pairing on each dot, and panel (c) the effective inter-dot exchange, all evaluated at fixed $\Gamma=0.5\Delta$. At this coupling rate, the system first undergoes the doublet-singlet transition, followed at larger U by the singlet-triplet transition. Despite the intricate in-gap spectrum, short chains already reproduce nearly all NRG levels; the lone exception is the first excited state in the large-U limit. For $\mathrm{ChE}(L=1)$ (ZBW), this triplet state is missed

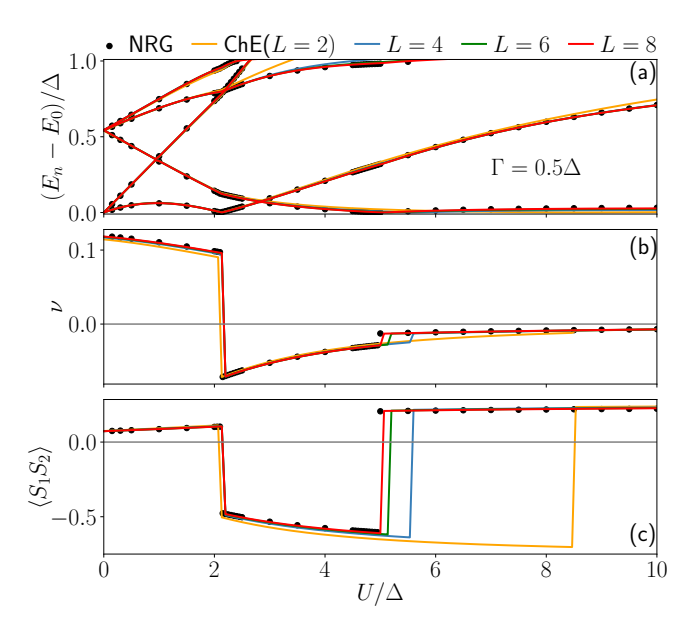


Figure 17. Parallel DQD coupled to a single lead illustrated in Fig. 15(a1). (a) In-gap excitation energies, (b) induced pairing $\nu = \langle d_{j\uparrow}^{\dagger} d_{j\downarrow}^{\dagger} \rangle$, and (c) spin correlations as functions of interaction strength U for $\Gamma = 0.5\Delta$ and $\zeta = 1$. Black circles denote NRG results, solid lines represent the corresponding ChE(L) predictions.

entirely, as discussed in Sec. III D and Ref. [35]. Extending the chain to $\mathrm{ChE}(L=2)$ removes that qualitative failure but still overestimates the critical U of the singlet-triplet transition. Only when L is sufficiently large, i.e., L=8, does the position of the QPT converge to the NRG benchmark, reflecting the small energy gap between the triplet ground state and the singlet first excited state at strong interactions.

Figure 18(a) plots the first-excited-state energy for several chain lengths L on a log-log scale. For L=1, small Γ and large U, an analytic expansion at half-filling shows that the lowest excitation is a triplet lying $\Delta E=3\times 16\Gamma^2/U^3$ above the singlet ground state (dashed red line). This positive splitting, generated by fourth-order tunneling processes in γ , yields an antiferromagnetic superexchange between the dots [92]. Removing the gap requires sixth-order virtual tunneling processes in \tilde{h}_ℓ that appear in the ChE basis only for chains of length $L\geq 2$.

The same trend is evident in the spin-spin correlators $\langle \hat{\mathbf{S}}_j \cdot \hat{\mathbf{s}}_\ell \rangle$ between a dot and chain site ℓ in Fig. 18(b). In the large-U limit, the sum over ℓ approximates the effective Kondo exchange. For L=1 the single term is strictly antiferromagnetic, so a triplet ground state cannot form [93]. When L>1, the sites with $\ell>1$ can add ferromagnetic contributions; at large U these are already strong enough for L=2 to favor the triplet, and longer chains shift the crossover to smaller U, converging on the true critical value. As we will discuss in the following sections, this limitation of ZBW is rather general, as it also

fails to predict the correct ground state for triple and quadruple QDs coupled to a common SC lead.

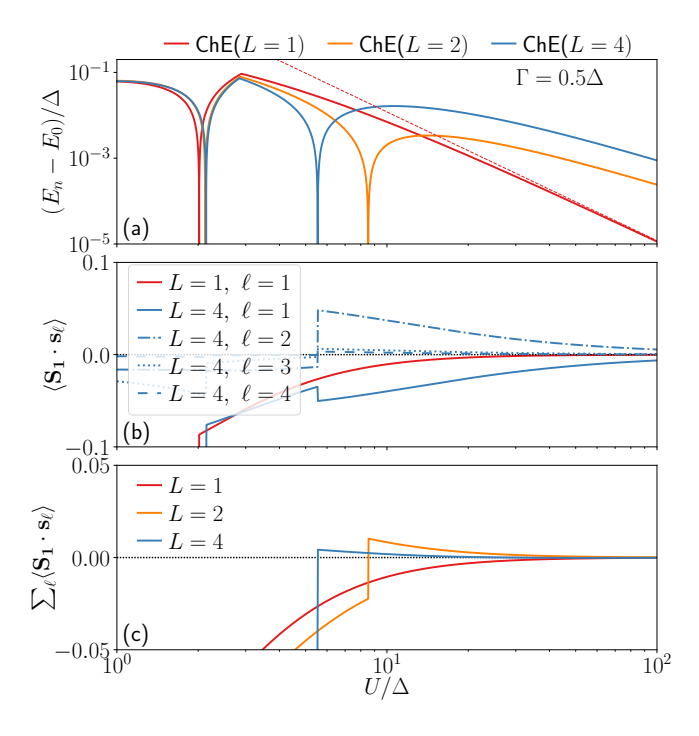


Figure 18. Parallel DQD coupled to a single lead illustrated in Fig. 15(a1). (a) First exited in-gap energy at $\Gamma=0.5\Delta$ for ChE(L=1,2,4). (b) Spin-spin correlations between the first QD and the ℓ th lead site. (c) Aggregated spin-spin correlations, showing that for L>1 the sum flips to positive values where the triplet emerges.

The phase diagram becomes even richer once the interdot capacitance is taken into account. Panels (a2) and (b2) of Fig. 16 show the same device with a finite $W=\Delta$. Under these conditions, the singlet sector splits into two distinct phases. In the admittedly non-physical limit U < W, the ground state is a charge singlet devoid of magnetic correlations. The detailed scan in Fig. 19 confirms that the two singlets are separated by a QPT at W=U. For W>U, the system favors a charge-ordered singlet in which one dot is predominantly doubly occupied while the other remains empty, giving rise to pronounced double occupancy [panel (b)] and vanishing spin correlation [panel (c)]. We note that a singlet-singlet QPT with similar properties was also predicted in serial DQDs [33].

Two distinct singlet ground states arise at half-filling even at W=0 once the system is detuned from the special point $\zeta=1$ ($\delta=0.5$); for $\delta\neq0.5$ two chains must be retained [see the illustration in Fig. 15(a2)]. Figure 20 shows examples of resulting phase diagrams. Panels (a1) and (a2) display the total spin in the $\Gamma-\delta$ plane for $U=\Delta$ and $U=10\Delta$, respectively, while panels (b1) and (b2) show the corresponding effective exchange. The origin of the two singlet regions in (a1) and (a2) is most transparent in the $\delta\to0$ limit, where the geometry

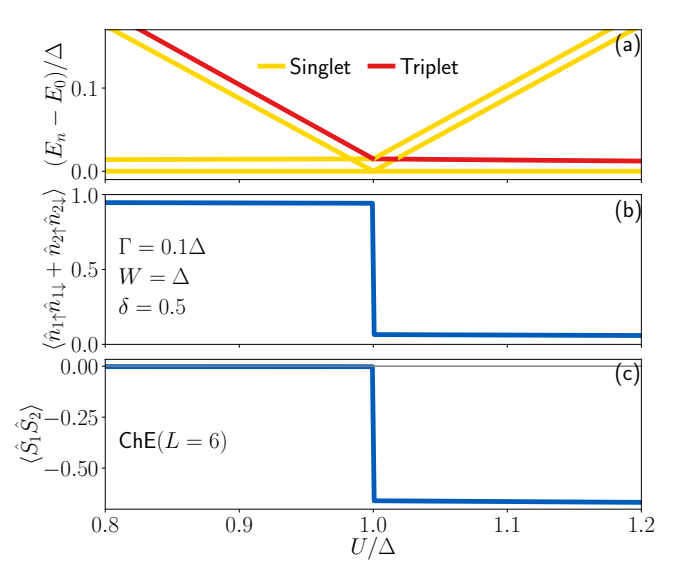


Figure 19. Evolution of low-energy properties across the singlet-singlet QPT in the DQD illustrated in Fig. 15(a1), obtained with ChE(L=6). (a) In-gap excitation energies, (b) double occupancy $\sum_j \langle n_{j\uparrow} n_{j\downarrow} \rangle$, and (c) inter-dot spin correlations, plotted as functions of U at $\Gamma=0.1\Delta$, $\zeta=1$ ($\delta=0.5$), and $W=\Delta$. Panel (a) shows the level crossing where the two singlet branches exchange order at the QPT. For U< W, the ground state is a singlet followed closely by the other singlet, whereas for U>W the ground-state singlet is followed by a triplet. The singlet-triplet splitting is proportional to Γ.

crosses over to a serial configuration. In this limit, each dot behaves almost independently; its single-dot (i.e., at each half separately) ground state can be either a singlet or a doublet with the phase diagram shown in Fig. 7. The two-dot device can therefore form two nonequivalent composite ground states built from the tensor products singlet \otimes singlet and doublet \otimes doublet [34].

The singlet \otimes singlet combination leads to a singlet composite ground state. However, the doublet \otimes doublet gives, without any correlations between the dots, a singlet-triplet degenerate ground state. An infinitesimal δ will lift the degeneracy by promoting singlet at weak U [Fig. 20 (a1)], or triplet at strong U [Fig. 20(a2)].

Note that the situation where both the ground state and first excited states are singlets is potentially interesting with respect to the recent proposal of YSR qubit [24]. Similarly, the stability of the triplet state down to $\delta\approx 0$ leads to interesting conclusions. The two-chain setup discussed above can also be viewed as a serial DQD device [Fig. 5] if δ is small. In this interpretation, direct interdot hopping is neglected ($t_d\approx 0$), while (small) cross couplings exist between the first lead and the second dot, and vice versa.

For a purely serial geometry ($\delta = 0$) with identical dots ($U_1 = U_2$, $\varepsilon_1 = \varepsilon_2$, $\Gamma_1 = \Gamma_2$), the ground state is always a singlet because any finite t_d splits the singlet-triplet pair by an exchange energy $\sim 4t_d^2/U$ [33, 34]. If, however, the cross couplings to the leads are allowed and t_d stays

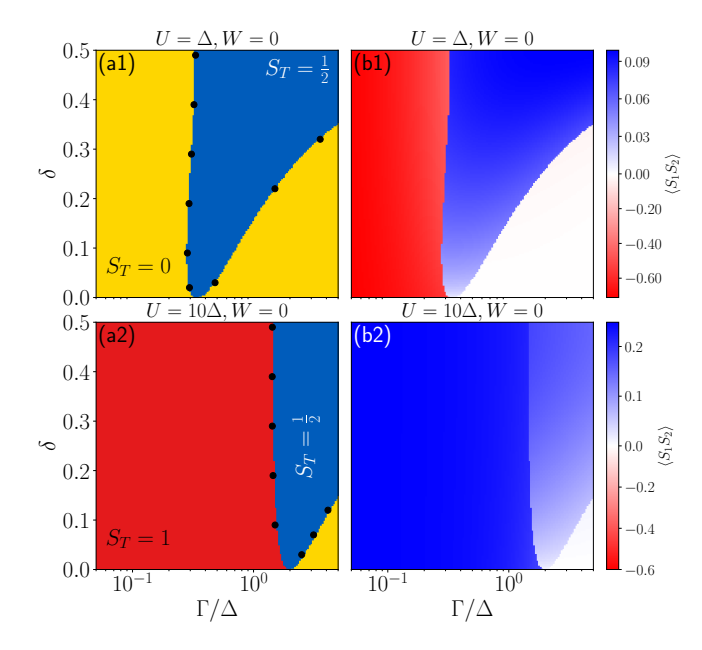


Figure 20. Phase diagrams for the DQD coupled to two SC chains, as illustrated in Fig. 15(a2), evaluated by CheE(L=2) and NRG (black circles) away from the maximally correlated point $\zeta=1$, where two chains are needed. (a1) Total spin S_T in the $\Gamma-\delta$ plane for symmetric dots, $\Gamma_1=\Gamma_2\equiv\Gamma$ and $U_1=U_2\equiv U=\Delta$, at half-filling with W=0. (b1) Corresponding average spin correlation $\langle \mathbf{S_1}\cdot\mathbf{S_2}\rangle$. (a2) Same as (a1) but for strong Coulomb interaction $U=10\Delta$. (b2) Mean spin correlation for the parameters of (a2).

small, a triplet ground state can emerge, as illustrated in Fig. 21. The finite t_d clearly suppresses the triplet phase, which is most stable near the triplet-doublet boundary, where a larger effective Γ helps to lock it in. It is important to note here that the half-filling is satisfied only approximately because the bipartite lattice condition is broken when both δ and t_d are finite.

B. Triple and Quadruple QD

Systems comprising three or more QDs have garnered growing interest, fueled by recent advances in the fabrication of ordered assemblies of magnetic atoms or molecules on SC surfaces [20, 22, 94, 95] as they represent tunable testbeds for studying various emerging phenomena. As an example, quadruple QDs are being explored for the interplay between Nagaoka ferromagnetism and the SC order [96]. Here, we offer what may be viewed as an entry-level systematic exploration of such complex systems. For clarity, we restrict ourselves to the fully local $\zeta = 1$ limit, i.e., each dot is coupled to a single SC chain in both the ChE and NRG treatments. The resulting phase diagrams in the $\Gamma - U$ plane at half-filling, shown in Fig. 22, resemble that of the DQD case both by the shape and number of ground state phases. Yet the individual phases differ markedly. For triple QD in panel

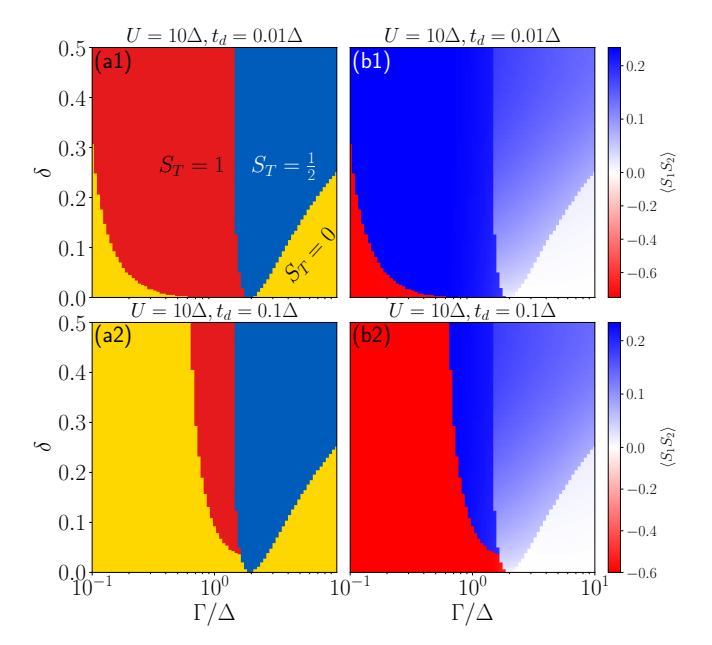


Figure 21. Phase diagrams for the DQD coupled to two SC leads, as illustrated in Fig. 15(a2), evaluated by ChE(L=2) away from the maximally correlated case $\zeta=1$, where two chains are needed. (a1) Total spin S_T in the $\Gamma-\delta$ plane for symmetric dots, $\Gamma_1=\Gamma_2\equiv\Gamma$ and $U_1=U_2\equiv U=10\Delta$, at half-filling with $t_d=0.01\Delta$ and W=0. (b1) Corresponding average spin correlation $\langle \mathbf{S}_1 \cdot \mathbf{S}_2 \rangle$. Panel (a2) is the same as (a1), but for $t_d=0.1\Delta$. (b2) Mean spin correlations for the same parameters as in (a2).

(a1), the dominant regions are a triplet ground state (red) that takes place above critical Γ and a quartet state $(S_T = 3/2, \text{ green})$ stable above critical U, with a doublet phase (blue) wedged between them in small Γ and weak to moderate U. For quadruple QD in panel (a2), the respective dominant regions are a quartet (green) ground state above critical Γ and a quintet state $(S_T = 2, \text{ black})$ above critical U, and the third phase is a singlet (yellow). Still, the magnetic diagrams in panels (b1) and (b2), are equivalent.

Another common feature of the double-, triple-, and quadruple-dot systems is the stability of the phase boundary, which extends from $U=0,\ \Gamma=0$ to large values of U and Γ . This boundary remains virtually unchanged as the chain length L is increased. Moreover, despite the intricate in-gap spectrum, a ChE description with only a few chain sites accurately reproduces the NRG excitation energies over several orders of magnitude in Γ , as demonstrated in Fig. 23. For weak interaction, $U=\Delta$, two sites (L=2) already suffice, and for $L\geq 4$ the ChE curves lie practically on top of the NRG results. The strong-coupling limit, $U=10\Delta$, is qualitatively simpler, but attaining the same accuracy as NRG demands a longer chain.

Finally, as in the DQD case, the ZBW approximation fails to capture the correct ground state in the small- Γ , large-U regime, regardless of the specific multiplet

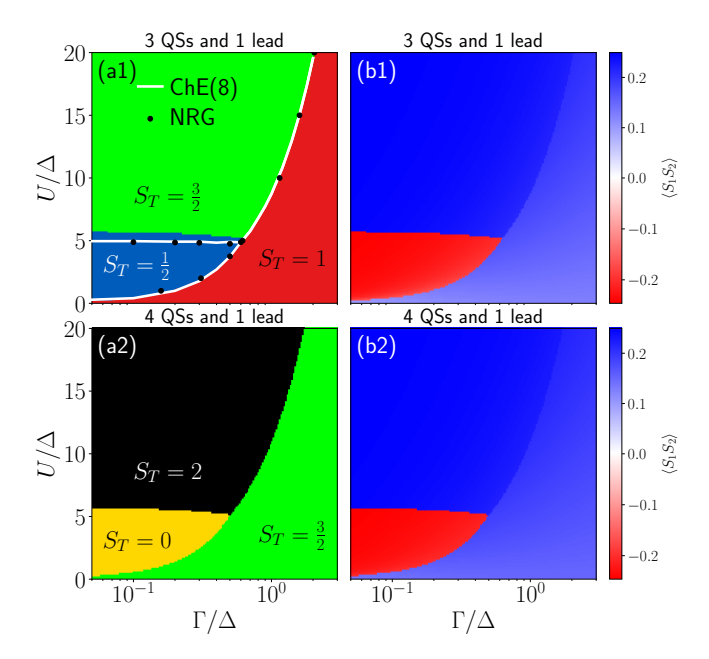


Figure 22. Phase diagrams for the triple (a) and quadruple (b) QD system with single SC lead as illustrated in Fig. 15(b) and (c). (a1) Total spin S_T in the $\Gamma - U$ plane for three symmetric dots at half-filling, W = 0, $t_d = 0$, and in the maximally correlated limit $\zeta = 1$. (b1) Corresponding average spin correlation $\langle \hat{\mathbf{S}}_1 \cdot \hat{\mathbf{S}}_2 \rangle$. (a2) Same as (a1) but for four dots coupled to the same chain. (b2) Mean spin correlation for the same parameters as in (a2). Phase boundaries (solid lines) computed with ChE(L) and critical points (black circles) obtained with NRG were determined from the positions of the QPT in the in-gap spectrum. Maps have been obtained with ChE(L = 4) and white boundaries in (a1) with ChE(L = 8).

involved. In this limit, the first excited state obtained with $\mathrm{ChE}(L=1)$ follows the same superexchange scaling, $\Delta E = b \times 16\Gamma^2/U^3$, with b=4 for the triple dot (doublet-quartet transition) and b=3 for the quadruple dot (singlet-quintet transition), as fitted to the numerical data in Fig. 24. This once again confirms that even for more complex systems, ZBW lacks the sixth-order virtual hopping processes in the lead needed to close the energy gap between the weak and strong U ground state phases and correctly reproduce the phase structure. This explains its consistent failure across all three geometries.

Another clear feature is the pronounced shift in the critical value of U that marks the transition from doublet to quartet in the triple dot, Fig. 24(a), and from singlet to quintet in the quadruple dot, Fig. 24(b), as the chain length L increases. This is evident from the position of the sharp minima at larger values of U in the difference between the first excited state and the ground state, corresponding to the crossing of the lowest eigenenergies. These minima shift significantly between L=2 (blue), L=3 (black) and L=4 (green) in Fig. 24. In contrast, the minima at smaller values of U remain stable for $L\geq 2$, indicating that the corresponding phase boundary has already converged.

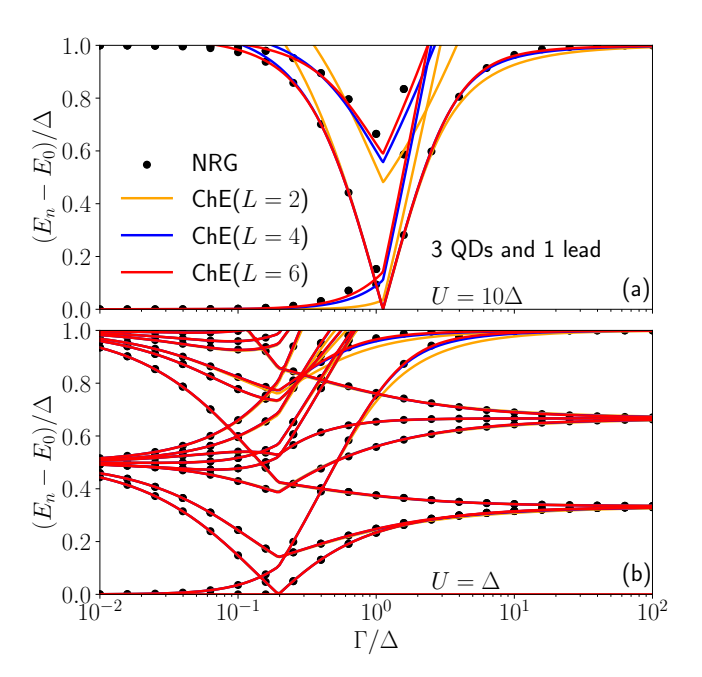


Figure 23. In-gap excitation energies for a triple QD coupled to a single SC lead as illustrated in Fig. 15(b) at $U=10\Delta$ (a) and $U=\Delta$ (b) calculated with NRG (black circles) and ChE(L) (solid lines) for different L.

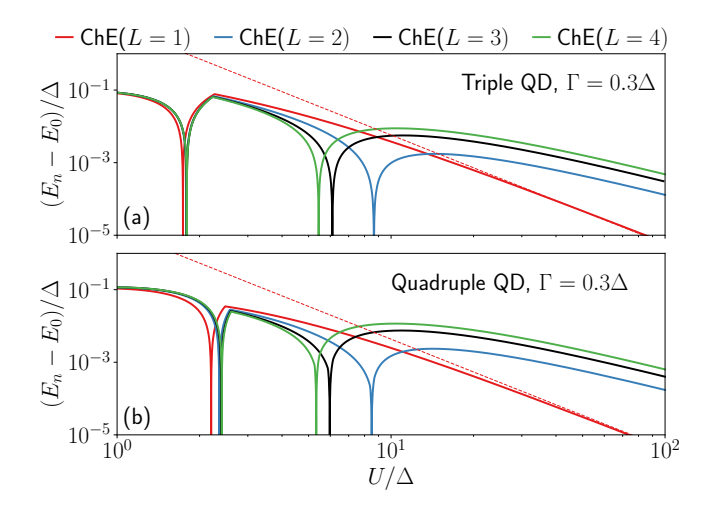


Figure 24. (a) First exited in-gap energy for $\Gamma=0.3\Delta$ for ChE(L=1,2,3,4) for triple QD coupled to a single SC lead, illustrated in Fig. 15(b). (b) First exited in-gap energy for $\Gamma=0.3\Delta$ for ChE(L=1,2,3,4) for quadruple QD coupled to a single SC lead, illustrated in Fig. 15(c). The dashed red lines show the strong U and weak Γ asymptotics described by $\Delta E=b\times 16\Gamma^2/U^3$ with b=4 for the triple QD and b=3 for the quadruple QD.

The inability of the ZBW approximation to capture the correct ground state becomes even more pronounced away from half-filling. In this regime, the phase diagrams become significantly more complex. For a triple dot, this is illustrated in Fig. 25, where we fix $\varepsilon_2 = 0$ and vary ε_1

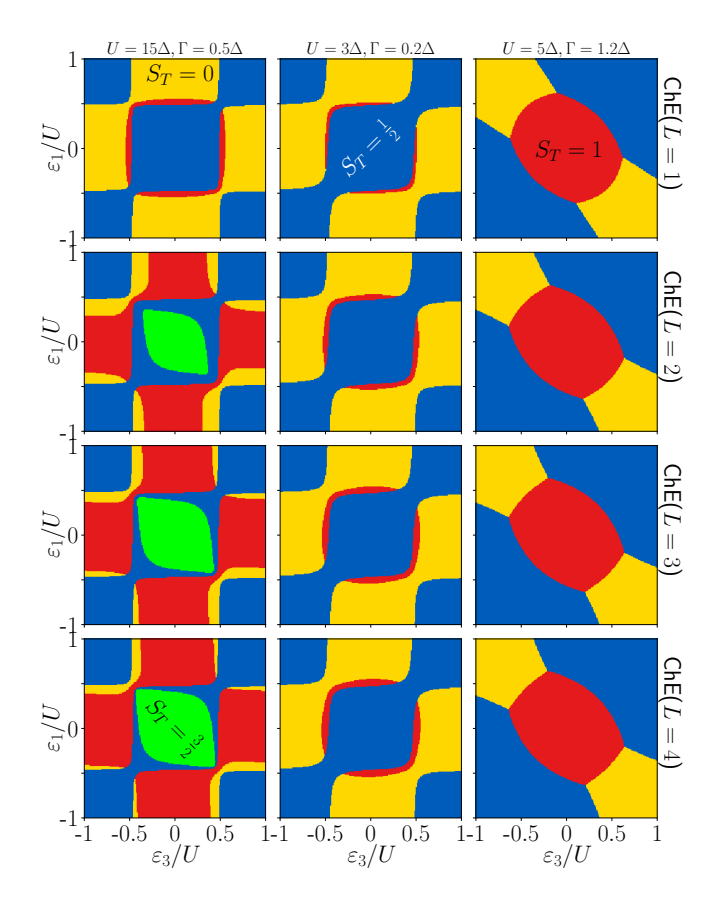


Figure 25. Phase diagrams for a triple QD coupled to a single SC lead illustrated in Fig. 15(b), evaluated away from half-filling. We fix $\varepsilon_2=0$ and vary ε_1 and ε_3 . Colors encode the total spin: $S_T=0$ (yellow), $S_T=1/2$ (blue), $S_T=1$ (red) and $S_T=3/2$ (green). The three columns correspond to different parameter sets: (i) $U=15\Delta$, $\Gamma=0.5\Delta$; (ii) $U=3\Delta$, $\Gamma=0.2\Delta$; and (iii) $U=5\Delta$, $\Gamma=1.2\Delta$, all with $t_d=0$ and W=0. These choices place the half-filled point in each of the three ground-state phases identified in Fig. 22(a). Rows display ChE results for increasing chain length: top, L=1; middle, L=2, and L=3; bottom, L=4.

and ε_3 . A noteworthy observation is that a singlet phase (yellow) – absent at half-filling – occupies a substantial portion of the diagram once particle-hole symmetry is broken.

For moderate interactions, such as $U = 3\Delta$, $\Gamma = 0.2\Delta$, and $U = 5\Delta$, $\Gamma = 1.2\Delta$, the ZBW phase boundaries agree well with those obtained from longer chains. In these regimes, ZBW proves reliable: the differences between L = 1 and L = 2 are minor, and larger values of L = 1 introduce only negligible corrections to the L = 2 case. However, in the strong-coupling limit $U = 15\Delta$, where the ground state at half filling is a quartet, the ZBW approximation fails even qualitatively. It completely misses the central $S_T = 3/2$ region (green) and significantly underestimates the extent of the surrounding triplet phase (red). While L = 2 provides qualitatively correct predictions, longer chains are necessary to accurately reproduce

the full phase diagram.

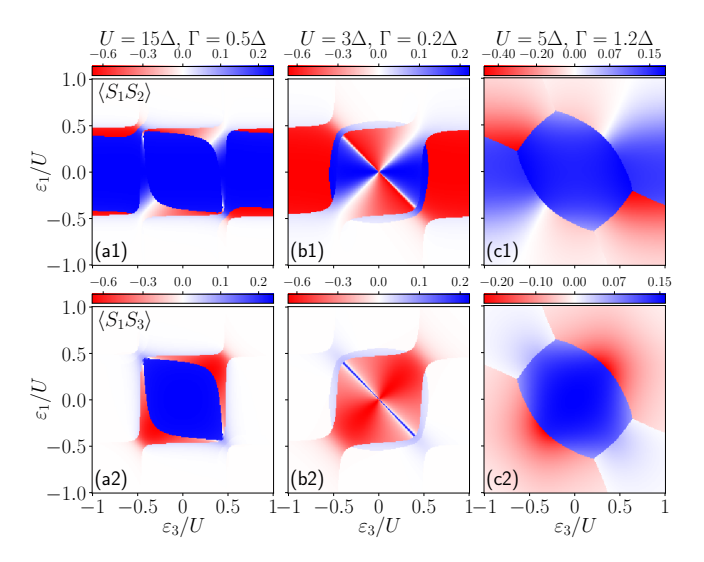


Figure 26. Triple QD coupled to a single SC lead illustrated in Fig. 15(b). Maps of spin correlations $\langle S_1 \cdot S_2 \rangle$ (first line) and $\langle S_1 \cdot S_3 \rangle$ (second line) for the same sets of parameters as phase diagrams in Fig. 25. Maps have been obtained using ChE(L=4).

1. Spin-spin correlations in triple QD

The structure of the ground state diagram is, in fact, richer than suggested by the total spin alone. Figure 26 shows spin-spin correlations, i.e., the effective magnetic exchange between the dots in the same setup as in Fig. 25. Specifically, it displays $\langle S_1.S_2 \rangle$ ($\langle S_3.S_2 \rangle$ is analogous) and $\langle S_1.S_3 \rangle$. These results reveal that identical total-spin ground states can exhibit very different magnetic correlations, not only between different pairs of dots (compare first and second line) but also for the same pair in different regions of the diagram.

A particularly interesting case occurs in the doublet ground state for $U=3\Delta$ and $\Gamma=0.2\Delta$. In this regime, spin correlations can vanish entirely in some regions of the diagram (e.g., the upper-left and lower-right corners), while in the central region – near half-filling – they exhibit a transition from strong ferromagnetic to strong antiferromagnetic character. The vanishing correlations arise from the QD fillings, as seen for $\varepsilon_3=-\varepsilon_1$. In this case, the total filling is 3, with the central dot occupied by one electron and the edge dots by approximately two and zero electrons, respectively. As a result, the spins on the edges are compensated, leading to zero spin correlations between the dots. The crossover in the central part of Fig. 26, which forms a distinctive "propeller-like" pattern in panel (b1), has a more complex origin.

This origin lies in the structure of the doublet ground state. For symmetric dots, i.e., $\varepsilon_1 = \varepsilon_2 = \varepsilon_3$, the ground state is doubly degenerate. Introducing asymmetry in

the level positions ε_i lifts this degeneracy, turning one of the doublets into the first excited state. This is illustrated in Fig. 27(a). Lines of different colors show different cuts for $\varepsilon_2 = 0$ and four fixed values of $\varepsilon_1 = 0$ (black), 0.001U (orange), 0.1U (blue) and 0.2U (red) and varying ε_3 . The sharp dips at the edges ($|\varepsilon_3| > 0.4U$) correspond to QPTs: singlet to triplet, and triplet to doublet. However, the only central minimum that approaches zero is the one for equal $\varepsilon_1 = \varepsilon_2 = 0$, where at $\varepsilon_3 = 0$ (black) two doublets meet. Nevertheless, even for this case, we have not identified a true QPT. The minima for $\varepsilon_3 \neq \varepsilon_2$ positioned at $\varepsilon_3 = -\varepsilon_1$ are accompanied by a sharp dip in spin correlations $\langle S_1 \cdot S_2 \rangle$ [orange line in panel (b)] for small ε_1 that becomes broader with increasing ε_1 . Analogously, the spin correlations $\langle S_1 \cdot S_3 \rangle$ shows an overshoot-undershoot type of behavior [orange line in panel (c) that gets broadened to a still relatively sharp peak at $\varepsilon_3 = -\varepsilon_1$ and broad dip at $\varepsilon_3 = \varepsilon_1$ with increasing ε_1 . These broadened shapes lead to regions with different effective exchange.

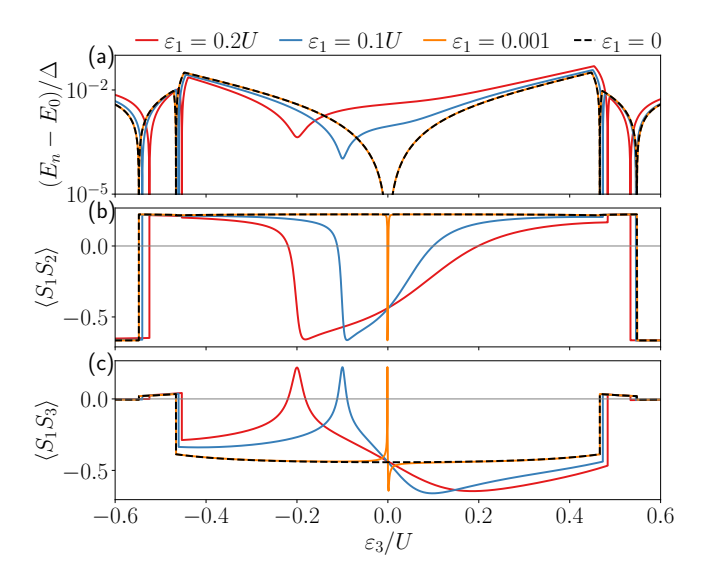


Figure 27. (a) First exited in-gap energy as a function of ε_3 for triple QD with single SC lead illustrated in Fig. 15(b), with $U=3\Delta$, $\Gamma=0.2\Delta$, $\varepsilon_2=0$ as in the panels (b1) and (b2) of Fig. 26 for $\epsilon_1=0.2U$ (red), 0.1U (blue), 0.001U (orange) and 0 (black). (b) The respective spin-spin correlations between first and second dot $\langle S_1 \cdot S_2 \rangle$ and (c) between the first and third dot $\langle S_1 \cdot S_3 \rangle$. The system was modeled by $\mathrm{ChE}(L=4)$.

To clarify this behavior, we applied a small magnetic field in the z direction. Its effect is described by the Hamiltonian.

$$H_B = -B_z \sum_{i=1}^{3} \left(n_{j\uparrow} - n_{j\downarrow} \right), \tag{24}$$

which further splits the ground state and first excited doublets of the $B_z = 0$ solution. Figure 28 shows the average z component of the spin on each dot (red, blue, and green lines) and their sum (black dashed line) as a

function of ε_3 for $\varepsilon_1=0.1\Delta$ and $B_z=10^{-5}\Delta$, for both the ground state (a) and the second excited state (b). The first excited state (not shown here) corresponds to the ground state with reversed spin polarities on each dot. In both panels (a) and (b), the sum of S^z is close to 1/2, indicating that only a small fraction of the spin resides in the lead. As in Fig. 27, two special points, $\varepsilon_3=\pm\varepsilon_1$, stand out: for $\varepsilon_3=\varepsilon_1$, $\langle S_2^z\rangle\approx 1/2$ while spins on the other two dots vanish, giving zero inter-dot correlations; for $\varepsilon_3=-\varepsilon_1$, a sharp negative peak in $\langle S_2^z\rangle$ is balanced by large positive values of $\langle S_2^z\rangle$ and $\langle S_3^z\rangle$. In the second excited state, this behavior is reversed.

These two points divide the central region into three regimes. For $\varepsilon_3<-\varepsilon_1$, the ordering is $\uparrow\uparrow\downarrow$, with effective ferromagnetic coupling between dots 1 and 2, and antiferromagnetic coupling between dot 3 and the other two. For $-\varepsilon_1<\varepsilon_3<\varepsilon_1$, the pattern is $\downarrow\uparrow\uparrow$; for $\varepsilon_3>\varepsilon_1$, it returns to $\uparrow\uparrow\downarrow$ but with reversed magnitudes of $\langle S_1^z\rangle$ and $\langle S_3^z\rangle$. Since the central region has width $2\varepsilon_1$, the transition sharpens as ε_1 decreases, with $\langle S_1^z\rangle$ and $\langle S_3^z\rangle$ converging. Even at $\varepsilon_1=0$, with only one special point, the ground and excited states do not exchange character as ε_3 crosses zero, so no true QPT is observed.

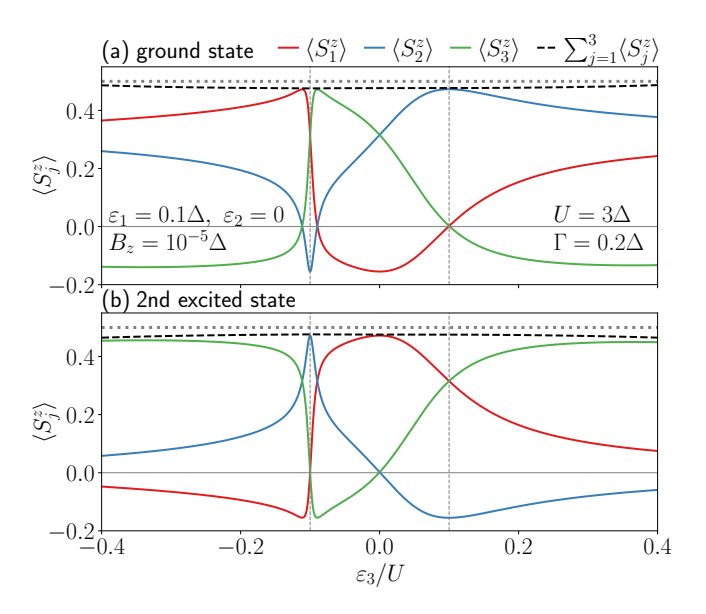


Figure 28. Triple QD coupled to a single SC lead illustrated in Fig. 15(b) with $U=3\Delta$, $\Gamma=0.2\Delta$, $\varepsilon_1=0.1\Delta$ and $\varepsilon_2=0$ in a weak magnetic field $B_z=10^{-5}\Delta$, which splits the doublet states. (a) Mean spin in the z direction for the ground state at each dot (red, blue, and green lines) and their sum (black dashed line). The horizontal gray solid line marks zero, while the dashed gray line indicates 1/2. Vertical dotted lines mark $\varepsilon_3=\varepsilon_1$ and $\varepsilon_3=-\varepsilon_1$. (b) Same as in (a), but for the second-excited state, i.e., the lower component of the split second doublet.

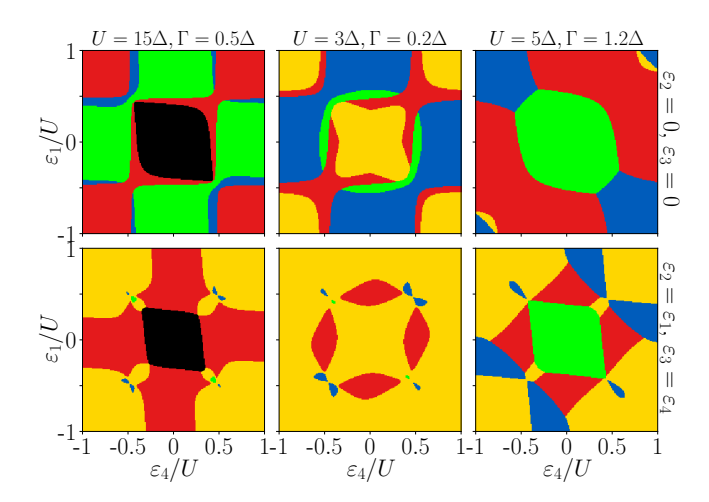


Figure 29. Phase diagrams for a quadruple QD coupled to a single SC lead, illustrated in Fig. 15(c), evaluated away from half-filling using ChE(L=4). In the first line we fix $\varepsilon_2=\varepsilon_3=0$ and vary ε_1 and ε_4 . The second line shows results where $\varepsilon_1=\varepsilon_2$ and $\varepsilon_3=\varepsilon_4$. Colors encode the total spin: yellow for $S_T=0$, blue for $S_T=1/2$, red for $S_T=1$, green for $S_T=3/2$ and black for $S_T=2$. The three columns correspond to the parameter sets (i) $U=15\Delta$, $\Gamma=0.5\Delta$; (ii) $U=3\Delta$, $\Gamma=0.2\Delta$; and (iii) $U=5\Delta$, $\Gamma=1.2\Delta$, all with $t_d=0$ and W=0.

2. Quadruple QD

The final results, shown in Fig. 29, present phase diagrams away from half filling for a quadruple dot using the same values of U and Γ studied in the double- and triple-dot cases. The first row shows cases where only the energy levels of the first and fourth dots are varied, with the other two kept at half-filling condition, i.e., $\varepsilon_2 = \varepsilon_3 = 0$. The second row explores a scenario in which tuning gates are applied symmetrically to pairs of neighboring dots, i.e., $\varepsilon_1 = \varepsilon_2$ and $\varepsilon_3 = \varepsilon_4$.

The resulting diagrams form a kaleidoscope of phases, with colors representing different total spin states. In addition to broad regions of singlet, doublet, triplet, quartet, and quintet phases (the latter seen in the leftmost panels), small, isolated pockets, not observed for double and triple dots, also appear in the diagrams. These regions are stable with respect to increasing chain length L (not shown here), indicating that they are robust features of the model. This illustrates how the addition of a single QD can generate qualitatively new behavior, consistent with the "more is different" concept [97]. It also highlights a key advantage of ChE over heavy numerical methods such as NRG or QMC. While detailed and reliable maps such as Fig. 25 can be obtained on standard PCs using ChE, achieving comparable results with NRG or QMC would require computational clusters and hundreds of node hours.

It is worth emphasizing that, for triple and quadruple dots coupled to a superconductor, this work represents an entry-level study. Realistic systems are far more complex, even within the already simplified framework of a generalized SC-AIM. Finite direct hopping and capacitive coupling between dots can be significant. The hybridization parameters V_{il} are, in general, complex. The spatial arrangement of the dots – for example, their relative positions on the SC substrate in an STM study – also plays a crucial role [20, 22]. Furthermore, effects such as Kondo screening, RKKY interaction, and superexchange can interfere in subtle ways. Exact numerical methods that account for all these ingredients remain prohibitively expensive for broad parameter scans. This underscores the need for approximate approaches that are nonetheless controlled, reliable, and scalable – such as the chain expansion scheme presented in this work

V. CONCLUSIONS

We have presented a chain-expansion scheme that builds low-energy effective models for SC heterostructures by expanding the tunneling self-energy into a finite tight-binding chain. The construction is flexible: different $Pad\acute{e}$ orders give chains of different lengths that can be chosen to match the task at hand.

Short $Pad\acute{e}$ chains containing only 2-4 sites already capture equilibrium properties in the typical parameter ranges. Because these Hamiltonians remain small, straightforward ED is fast enough to scan broad phase spaces, even for complicated multi-dot layouts. Increasing the chain length L improves the accuracy in a controlled way, and they work equally well out of equilibrium, where they agree with NEGF calculations.

Using $\mathrm{ChE}(L)$, we mapped the ground-state phase diagrams of double, triple, and quadruple dots coupled to a single SC lead. We demonstrated that at the half-filling, these phase diagrams have similar overall shapes but consist of different ground-state phases. Particularly interesting is the regime of large U and small Γ . Here, the ZBW limit, a heavily used effective model, fails to give the correct ground state. Longer chains correctly capture these phases, but lengths up to L=4 are typically needed to pinpoint the position of the relevant QPT.

For the double dot, we show that capacitive coupling can drive a singlet-singlet QPT. We also varied the strength of the lead-mediated inter-dot pairing. Depending on the other parameters, a relatively weak pairing can stabilize triplet ground states even when direct hopping between dots is present.

Moving away from half-filling makes the phase diagrams more complex, especially for a larger number of dots. We show that although the ZBW approximation can still be reliable in some regimes, it often predicts qualitatively incorrect ground states.

We presented ChE not just as a model but also as a general strategy. Like NRG or the recently proposed surrogate models, it replaces the lead by a finite or semi-infinite chain. Its main advantages, as presented here, are that the chains are built using $Pad\acute{e}$ approximants;

therefore, they are the optimal low-energy representations to a given $Pad\acute{e}$ order. We supplied an algorithm for arbitrary bandwidth and simple analytic formulas for WBL and the infinite-chain limit. Very short chains give quantitative results with ED; longer chains are still manageable by (t)DMRG or Monte Carlo methods, letting one tackle multi-terminal and time-dependent problems. ChE chains can also be combined with other approaches, such as Wilson chains, where the main channel is treated by NRG and a side-coupled short ChE chain captures additional channels. In addition, the accuracy of ChE schemes makes them suitable substitutes for other, more demanding impurity solvers and can eventually be used to treat lattice models like the SC periodic Anderson model within the dynamical mean-field theory [49, 98]. Finally, the only convergence parameter in the presented scheme is the chain length L, providing a controllable alternative to methods that require non-trivial parameter fitting and advanced discretization schemes.

In this way, ChE offers not just another method, but a practical and broadly adaptable framework for advancing the study of strongly correlated superconducting systems.

ACKNOWLEDGMENTS

The authors acknowledge support from the Czech Science Foundation through project No. 23-05263K. This work was also supported by the Ministry of Education, Youth and Sports of the Czech Republic through the e-INFRA CZ (ID:90254), the Czech Republic-Germany Mobility programme (ID:8J25DE001), and EU COST

action CA21144 SUPERQUMAP. We thank Artur Slobodeniuk, Peter Zalom, Tomáš Novotný, and Wolfgang Belzig for many productive discussions.

Appendix A: Tunneling self-energy of ChE model as a continued fraction

To obtain the dot Green's function for the ChE models from its all-sites form in Eq. (9), which is equivalent to the full SC-AIM analogue of Eq. (5), we must integrate out the states that belong to the chain. A convenient way is to eliminate them iteratively using a block-matrix identity [99]

$$\begin{pmatrix} \mathbf{A} & \mathbf{c} \\ \mathbf{d} & \mathbf{B} \end{pmatrix}^{-1} = \begin{pmatrix} (\mathbf{A} - \mathbf{c} \mathbf{B}^{-1} \mathbf{d})^{-1} & -\mathbf{A}^{-1} \mathbf{c} (\mathbf{B} - \mathbf{d} \mathbf{A}^{-1} \mathbf{c})^{-1} \\ -\mathbf{B}^{-1} \mathbf{d} (\mathbf{A} - \mathbf{c} \mathbf{B}^{-1} \mathbf{d})^{-1} & (\mathbf{B} - \mathbf{d} \mathbf{A}^{-1} \mathbf{c})^{-1} \end{pmatrix},$$
(A1)

Due to the pentadiagonal structure, we can formally apply the above identity successively to the 2×2 Ablocks, starting from the upper left corner of the matrix in Eq. (9), one block at a time. After this formal forward sweep, we get a ladder of auxiliary matrices \mathcal{A} that can be calculated in reverse order by taking advantage of the identity

$$\sigma_z \begin{pmatrix} i\omega_n & \widetilde{\Delta} \\ \widetilde{\Delta} & i\omega_n \end{pmatrix}^{-1} \sigma_z = \frac{-1}{\omega_n^2 + \widetilde{\Delta}^2} \begin{pmatrix} i\omega_n & \widetilde{\Delta} \\ \widetilde{\Delta} & i\omega_n \end{pmatrix} \equiv \frac{-1}{\omega_n^2 + \widetilde{\Delta}^2} \mathbb{A},$$
(A2)

where σ_z is the third Pauli matrix. The series then reads

$$\begin{split} \mathcal{A}_{L-1}^{-1} &= \left(\mathbb{A} - \widetilde{h}_{L-1}^2 \sigma_z \mathbb{A}^{-1} \sigma_z\right)^{-1} = \left(\mathbb{A} + \widetilde{h}_{L-1}^2 (\widetilde{\Delta}^2 + \omega_n^2)^{-1} \mathbb{A}\right)^{-1} = (\widetilde{\Delta}^2 + \omega_n^2) (\widetilde{\Delta}^2 + \widetilde{h}_{L-1}^2 + \omega_n^2)^{-1} \mathbb{A}^{-1}, \\ \mathcal{A}_{L-2}^{-1} &= \left(\mathbb{A} - \widetilde{h}_{L-2}^2 \sigma_z A_{L-1}^{-1} \sigma_z\right)^{-1} = \left(1 + \widetilde{h}_{L-2}^2 (\widetilde{\Delta}^2 + \widetilde{h}_{L-1}^2 + \omega_n^2)^{-1}\right)^{-1} \mathbb{A}^{-1}, \\ \mathcal{A}_{L-3}^{-1} &= \left(\mathbb{A} - \widetilde{h}_{L-3}^2 \sigma_z A_{L-2}^{-1} \sigma_z\right)^{-1} = (\widetilde{\Delta}^2 + \omega_n^2) \left(\widetilde{\Delta}^2 + \omega_n^2 + \widetilde{h}_{L-3}^2 \left(1 + \widetilde{h}_{L-2}^2 (\widetilde{\Delta}^2 + \widetilde{h}_{L-1}^2 + \omega_n^2)^{-1}\right)^{-1}\right)^{-1} \mathbb{A}^{-1}, \\ \mathcal{A}_{L-4}^{-1} &= \left(1 + \widetilde{h}_{L-4}^2 \left(\widetilde{\Delta}^2 + \omega_n^2 + \widetilde{h}_{L-3}^2 \left(1 + \widetilde{h}_{L-2}^2 (\widetilde{\Delta}^2 + \widetilde{h}_{L-1}^2 + \omega_n^2)^{-1}\right)^{-1}\right)^{-1} \mathbb{A}^{-1}, \\ &: \end{split}$$

There are two important observations here. The first is that the matrix structure is preserved solely by A. The

second is that the prefactor is clearly a continuous fraction. When rolled up to the QD, the prefactor reads

$$\widetilde{\mathcal{P}}(\omega_n; \widetilde{\Delta}, \gamma, \{\widetilde{h}_\ell\}) = \frac{\gamma^2}{\widetilde{\Delta}^2 + \omega_n^2 + \frac{\widetilde{h}_1^2}{1 + \frac{\widetilde{h}_2^2}{\widetilde{\Delta}^2 + \omega_n^2 + \frac{\widetilde{h}_2^2}{1 + \frac{\widetilde{h}_2^2}{\widetilde{\Delta}^2 + \omega_n^2 + \frac{\widetilde{h}_2^2}{1 + \frac{\widetilde{h}_2^2}{\widetilde{\Delta}^2 + \omega_n^2 + \frac{\widetilde{h}_2^2}{1 + \frac{\widetilde{h}_2^2}{\widetilde{h}_2^2}}}}.$$
(A3)

The continued fraction terminates with $(\widetilde{\Delta}^2 + \omega_n^2 + \widetilde{h}_{L-1}^2)$ for a chain with an even number of sites and with $(1 + \widetilde{h}_{L-1}^2)$ $\widetilde{h}_{L-1}^2/(\widetilde{\Delta}^2+\omega_n^2)$ in the case of an odd number of sites.

This leads to the non-interacting dot Green's function that reads

$$G_{U=0}^{\text{ChE(L)}} = \begin{pmatrix} i\omega_n \left[1 + \widetilde{\mathcal{P}} \left(\omega_n; \widetilde{\Delta}, \gamma, \{\widetilde{h}_\ell\} \right) \right] - \epsilon & \widetilde{\Delta} \widetilde{\mathcal{P}} \left(\omega_n; \widetilde{\Delta}, \gamma, \{\widetilde{h}_\ell\} \right) \\ \widetilde{\Delta} \widetilde{\mathcal{P}} \left(\omega_n; \widetilde{\Delta}, \gamma, \{\widetilde{h}_\ell\} \right) & i\omega_n \left[1 + \widetilde{\mathcal{P}} \left(\omega_n; \widetilde{\Delta}, \gamma_n, \{\widetilde{h}_\ell\} \right) \right] + \epsilon \end{pmatrix}^{-1}.$$
(A4)

After the rescaling introduced in Eq. (10), repeated here for convenience

$$\gamma = \sqrt{\frac{\Gamma}{\Delta}h_0}\Delta, \qquad \widetilde{h}_\ell = \sqrt{h_\ell}\Delta, \tag{A5}$$

the comparison of Eq. (A4) with Eq. (5) sets $\widetilde{\Delta}$ = Δ and gives the dot Green's function Eq. (11) where $\mathcal{P}_L(\frac{\omega_n}{\Lambda}; \{h_\ell\})$ is a finite continued fraction

$$\mathcal{P}\left(\frac{\omega_{n}}{\Delta}; \{h_{\ell}\}\right) = \frac{h_{0}}{1 + \frac{\omega_{n}^{2}}{\Delta^{2}} + \frac{h_{1}}{1 + \frac{h_{2}}{\Delta^{2}} + \frac{h_{3}}{1 + \frac{\omega_{n}^{2}}{\Delta^{2}} + \frac{h_{3}}{1 + \frac{\omega_{n}^{2}}{\Delta^{2}} + \frac{h_{5}}{1 + \frac{h_{6}}{\Delta^{2}}}}.$$
(A6)

Therefore, it can be expressed using the matrix product form as $\mathcal{P}_L(x;\{h_\ell\}) = P_L/Q_L$, where

$$\begin{pmatrix} P_L \\ Q_L \end{pmatrix} = \prod_{\ell=0}^{L-1} \begin{pmatrix} 0 & h_{\ell} \\ 1 & (1 + [(\ell+1) \mod 2] x^2) \end{pmatrix} \begin{pmatrix} 0 \\ 1 \end{pmatrix}, \text{ (A7)} \qquad \mathcal{P}_L(x; \{h_{\ell}\}) = \frac{1}{1+x^2} \frac{\sum_{j=0}^{(L-1)/2} p_j(\{h_{\ell}\}) x^{2j}}{\sum_{j=0}^{(L-1)/2} q_j(\{h_{\ell}\}) x^{2j}}$$

leading to the rational functions (Eqs. (12) and (13) in the main text)

$$\mathcal{P}_L(x;\{h_\ell\}) = \frac{\sum_{j=0}^{L/2-1} p_j(\{h_\ell\}) x^{2j}}{\sum_{j=0}^{L/2} q_j(\{h_\ell\}) x^{2j}}$$
(A8)

for even L and

$$\mathcal{P}_L(x;\{h_\ell\}) = \frac{1}{1+x^2} \frac{\sum_{j=0}^{(L-1)/2} p_j(\{h_\ell\}) x^{2j}}{\sum_{j=0}^{(L-1)/2} q_j(\{h_\ell\}) x^{2j}}$$
(A9)

for odd L.

The calculation of h_{ℓ} therefore differs slightly between chains with even and odd numbers of sites L. In what follows, we use Δ as an energy unit. For even L the

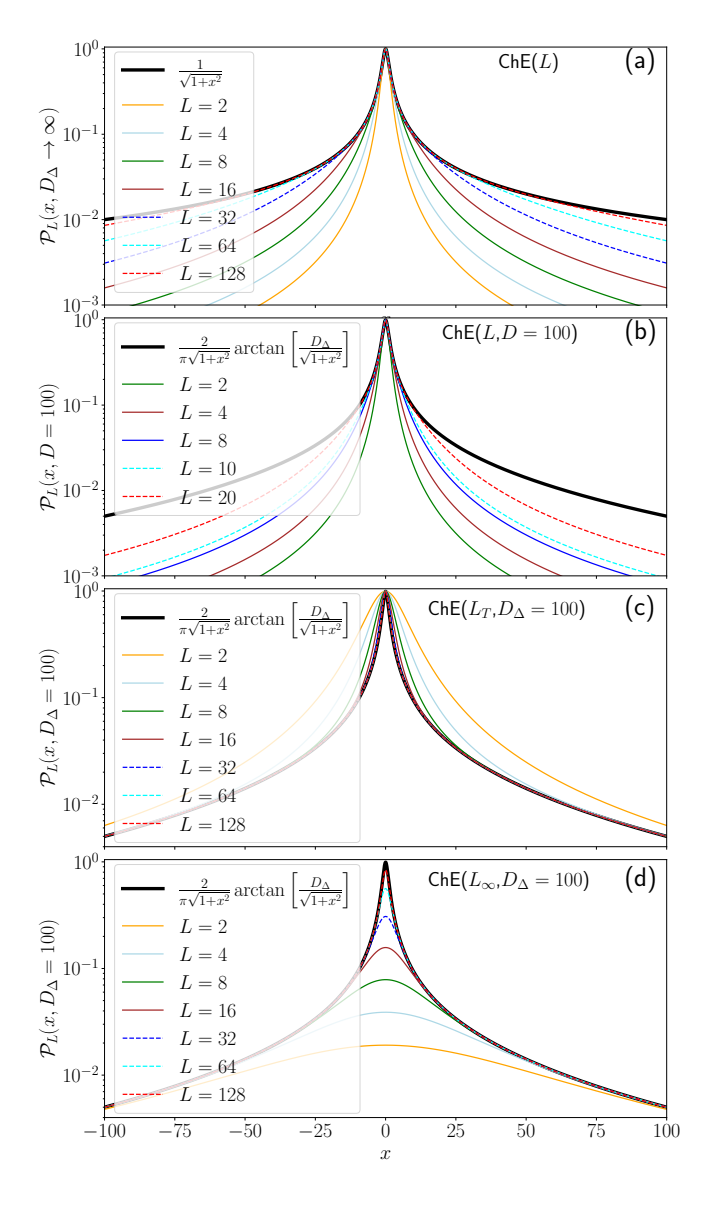


Figure 30. Comparison of the approximate function $\mathcal{P}_L(x,h_\ell)$ with the full hybridization function $\widetilde{\Gamma}(\omega_n;D)$ for $\Delta=1$. (a) WBL, where the coefficients h_ℓ take the simple analytic form given in Eq.(17). (b) Finite-bandwidth case with $D_\Delta=100$, where h_ℓ are obtained using the method described in the main text and Appendix A, based on matching the $Pad\ell$ approximant to the full tunneling self-energy. (c) Truncated expansion of the infinite-chain model, where the last coefficient is evaluated using Eq. (A29), with $D_\Delta=100$. (d) Truncated infinite-chain expansion for $D_\Delta=100$, without applying the correction to the final coefficient.

needed Padé expansion reads

$$\frac{1}{\sqrt{1+x^2}} \frac{2}{\pi} \arctan \left[\frac{D}{\sqrt{1+x^2}} \right] \approx \frac{\sum_{j=0}^{L/2-1} p_j x^{2j}}{\sum_{j=0}^{L/2} q_j x^{2j}}, \quad (A10)$$

for odd L we use the $Pad\acute{e}$ approximant for the expression

in the curly brackets

$$\frac{1}{1+x^2} \left\{ \frac{2}{\pi} \sqrt{1+x^2} \arctan\left[\frac{D}{\sqrt{1+x^2}}\right] \right\}
\approx \frac{1}{(1+x^2)} \frac{\sum_{j=0}^{(L-1)/2} p_j x^{2j}}{\sum_{j=0}^{(L-1)/2} q_j x^{2j}}, \tag{A11}$$

We now transform these expressions to a standard rational polynomials using:

$$\overline{p}_k = \sum_{j=k}^{N-1} {j \choose k} (-1)^{j-k} p_j, \quad \widetilde{p}_k = \overline{p}_k / \overline{q}_N,
\overline{q}_k = \sum_{j=k}^{N} {j \choose k} (-1)^{j-k} q_j, \quad \widetilde{q}_k = \overline{q}_k / \overline{q}_N$$
(A12)

with N = L/2 for even L and

$$\overline{p}_k = \sum_{j=k}^{N-1} {j \choose k} (-1)^{j-k} p_j, \quad \widetilde{p}_k = \overline{p}_k / \overline{q}_N,
\overline{q}_{k+1} = \sum_{j=k}^{N-1} {j \choose k} (-1)^{j-k} q_j, \quad \widetilde{q}_k = \overline{q}_k / \overline{q}_N$$
(A13)

with N=(L-1)/2+1 and $\overline{q}_0=0$ for odd L. By applying the substitution $z=1+x^2$ we get the standard rational polynomials, which allows us to use some continued fraction identities

$$\mathcal{R}(z) = \frac{\sum_{k=0}^{N-1} \widetilde{p}_k z^k}{\sum_{k=0}^{N} \widetilde{q}_k z^k}.$$
 (A14)

The rest of the solution is the same for odd and even L, because the above manipulation allows us to rewrite the fraction Eq. (A6) as

$$\frac{h_0}{z} + \frac{h_1}{1} + \frac{h_2}{z} + \frac{h_3}{1} + \frac{h_4}{z} \dots \tag{A15}$$

The coefficients h_{ℓ} are calculated by the method outlined in Ref. [83] using the odd (M_j^o) and even (M_j^e) (not related to odd and even L) principal minors, i.e., the determinants of the sub-matrices

where \widetilde{p}_j and \widetilde{q}_j with j<0 are zero and we also need $M_0^o=\widetilde{q}_N=1$ and $M_0^e=1$. The coefficients h_ℓ are then

$$h_0 = \frac{M_1^o}{M_0^o}, \ h_{2j-1} = \frac{M_{j-1}^o M_j^e}{M_j^o M_{j-1}^e}, \ h_{2j} = \frac{M_{j+1}^o M_{j-1}^e}{M_j^o M_j^e},$$
(A17)

where j > 0. Examples for $ChE(L = 1, D_{\Delta})$ (ZBW) and $ChE(L = 2, D_{\Delta})$ (eZBW) can be found in the main text. For WBL $(D_{\Delta} \to \infty)$ this leads to Eq. (17).

a. Examples:

To illustrate the procedure for determining the coefficients of $\text{ChE}(L, D_{\Delta})$, we present two simple step-by-step examples for L=3 with finite band width and L=4 for the WBL.

We begin with the less intuitive case of odd L, represented here by L=3 and $D_{\Delta}=10$. For odd L, we use the $Pad\acute{e}$ [(L-1)/(L-1)] form, as shown in Eq. (A12), applied only to the term in the curly brackets, rather than to the entire expression. For L=3 we need $Pad\acute{e}$ [2/2] which leads to

$$\frac{1}{1+x^2} \left\{ \sqrt{1+x^2} \frac{2}{\pi} \arctan\left[\frac{10}{\sqrt{1+x^2}}\right] \right\} \approx
\approx \frac{1}{1+x^2} \frac{0.936549 + 0.704351x^2}{1.+0.285722x^2}.$$
(A18)

Therefore, we identify $p_0 \doteq 0.936549$, $p_1 \doteq 0.704351$, $q_0 = 1$, and $q_1 \doteq 0.285722$. Using the coefficient transformation formulas for odd-site chains, we find the normalized coefficients

$$\widetilde{p}_0 = (p_0 - p_1)/q_1, \quad \widetilde{p}_1 = p_1/q_1,
\widetilde{q}_0 = 0, \quad \widetilde{q}_1 = (q_0 - q_1)/q_1, \quad \widetilde{q}_2 = 1,$$
(A19)

which allows us to construct the matrix (A16),

$$\begin{pmatrix}
\widetilde{p}_1 & \widetilde{p}_0 & 0 \\
\widetilde{q}_2 & \widetilde{q}_1 & \widetilde{q}_0 \\
0 & \widetilde{p}_1 & \widetilde{p}_0
\end{pmatrix}.$$
(A20)

The required minors (subdeterminants), therefore, read

$$M_0^e = M_0^o = 1,$$

$$M_1^o = \widetilde{p}_1,$$

$$M_1^e = \widetilde{p}_1 \widetilde{q}_1 - \widetilde{p}_0 \widetilde{q}_2,$$

$$M_2^o = \widetilde{p}_0 M_1^e.$$
(A21)

Using Eq. (A17) we finally get the h coefficient values as

$$\begin{split} h_0 &= \widetilde{p}_1 \doteq 2.46516, \\ h_1 &= (\widetilde{p}_1 \widetilde{q}_1 - \widetilde{p}_0 \widetilde{q}_2) / \widetilde{p}_1 \doteq 2.17024, \\ h_2 &= \widetilde{p}_0 / \widetilde{p}_1 \doteq 0.329662. \end{split} \tag{A22}$$

For the even L and WBL we calculate the $Pad\acute{e}$ approximant [L-2/L] of the self energy function $1/\sqrt{1+x^2}$. Taking as an example the case L=4, and therefore $Pad\acute{e}$ approximant [2,4], we get

$$\frac{1}{\sqrt{1+x^2}} \approx \frac{1 + \frac{1}{2}x^2}{1 + x^2 + \frac{1}{8}x^4},\tag{A23}$$

which gives coefficients $p_0 = 1, p_1 = \frac{1}{2}, q_0 = 1, q_1 = 1$, and $q_2 = \frac{1}{8}$. Using the coefficient transformation formulas for even-site chains, we find the normalized coefficients

$$\widetilde{p}_0 = 4, \qquad \widetilde{p}_1 = 4,
\widetilde{q}_0 = 1, \qquad \widetilde{q}_1 = 6, \qquad \widetilde{q}_2 = 1.$$
(A24)

Now we substitute the values of \widetilde{p}_k and \widetilde{q}_k into the matrix (A16) and calculate the needed minors

$$M_0^o = 1, \ M_0^e = 1,$$

 $M_1^o = 4, \ M_1^e = 20,$
 $M_2^o = 64, \ M_2^e = 64.$ (A25)

Finally, we use the Eq. (A17) to calculate coefficients h_l obtaining

$$h_0 = 4, \quad h_1 = 5, \quad h_2 = 4/5, \quad h_3 = 1/5.$$
 (A26)

These values are in agreement with the Eq. (17) for L=4

b. Infinite L limit:

For very long chains $(L \gg 1)$, it is advantageous to use the result for the infinite L, which follows directly from the continued fraction expansion of the arctan function,

$$\frac{2}{\pi} \frac{1}{\sqrt{1+x^2}} \arctan \left[\frac{D_{\Delta}}{\sqrt{1+x^2}} \right] = \frac{2D_{\Delta}/\pi}{1(1+x^2) + \frac{(1D_{\Delta})^2}{3 + \frac{(2D_{\Delta})^2}{5(1+x^2) + \frac{(3D_{\Delta})^2}{7 + \frac{(4D_{\Delta})^2}{9(1+x^2) + \frac{(5D_{\Delta})^2}{\vdots}}}}$$

after straightforward rearrangement of this continued fraction to the form of Eq. (A6) we can directly read the coefficients for $L \to \infty$:

$$h_0 = \frac{2}{\pi} D_{\Delta}, \qquad h_{\ell} = \frac{\ell^2 D_{\Delta}^2}{(2\ell+1)(2\ell-1)}.$$
 (A28)

For finite lattices, we truncate the series by assuming x=0 for all terms with $h_{\ell>L-1}$ and evaluate the resulting infinite continued fraction

$$h_{L-1} = \frac{\frac{(L-1)^2 D_{\Delta}^2}{4(L-1)^2 - 1}}{1 + \frac{\frac{L^2 D_{\Delta}^2}{4(L^2 - 1)}}{1 + \frac{\frac{(L+1)^2 D_{\Delta}^2}{4(L+1)^2 - 1}}{1 + \frac{\frac{(L+1)^2 D_{\Delta}^2}{4(L+2)^2 - 1}}{1 + \frac{\frac{(L+2)^2 D_{\Delta}^2}{4(L+3)^2 - 1}}{1 + \frac{(L+3)^2 D_{\Delta}^2}{4(L+3)^2 - 1}}}$$

$$\vdots \qquad (A29)$$

to get h_{L-1} that improves the approximation for small x. Note that the coefficients of $ChE(L, D_{\Delta})$ approach the special limits of ChE(L) and $ChE(L_{\infty}, D_{\Delta})$ as expected.

Appendix B: Systems with multiple leads coupled to the same QD

Representing each SC lead by its own chain is straightforward and works even for unequal leads, i.e., with different superconducting gaps or chemical potentials, or leads coupled to multiple dots. However, when multiple leads are coupled to the same QD and not to any other dot, all such leads can be represented by a single chain. This construction relies on the geometric factor χ_j introduced in Ref. [38] and its generalization to multi-dot systems discussed in Appendix VI of that work. In these cases, the tunneling self-energies are block diagonal with 2×2 Nambu blocks

$$\Sigma_{j}(\omega_{n}) = \begin{pmatrix} i\omega_{n} \frac{1}{\Delta}, & \chi_{j} \\ \chi_{j}^{*} & i\omega_{n} \frac{1}{\Delta} \end{pmatrix} \Gamma_{jT} \widetilde{\Gamma}(\omega_{n}; D),$$
 (B1)

which describes the local coupling of dot j to all its leads. Here, the complex geometric factor is

$$\chi_j = \sum_{\ell} \gamma_{j\ell} e^{i\varphi_{j\ell}} \tag{B2}$$

where $\Gamma_{jT} = \sum_{\ell} \Gamma_{j\ell}$ is the total coupling constant to dot j and $\gamma_{j\ell} = \Gamma_{j\ell}/\Gamma_{jT}$. Writing $\chi_j = \chi_j e^{i\Phi_j}$, the amplitude $\chi_j \in \langle 0, 1 \rangle$ and phase Φ_j characterize the net pairing. By gauge invariance, all $\varphi_{j\ell}$ can be shifted by a constant so that one Φ_j (e.g., for j=1) is set to zero, making $\chi_1 = \chi_1$ real [38].

A single-chain expansion (sChE) effective model that reproduces the self-energy (B1) for block j can be set as

$$\mathcal{H}^{\chi_j} = -\sqrt{h_0 \Gamma_{jT} \Delta} \sum_{\sigma} \left(e^{i\Phi_j/2} d^{\dagger}_{j\sigma} c_{1j\sigma} + \text{H.c.} \right)$$
$$- \Delta \sum_{\ell=1}^{L-1} \sum_{\sigma} \left(\sqrt{h_{\ell}} c^{\dagger}_{\ell j\sigma} c_{\ell+1,j\sigma} + \text{H.c.} \right)$$
$$- \chi_j \Delta \sum_{\ell=1}^{L} \left(c^{\dagger}_{\ell j\uparrow} c^{\dagger}_{\ell j\downarrow} + \text{H.c.} \right),$$
(B3)

with coefficients h_ℓ obtained by the same procedure as in the main text or by the algorithm in Appendix A (with minor modifications, e.g., the substitution $z=\chi_j^2+x^2$ which also changes the transformation factor $(-1)^{j-k}$ to $(-\chi^2)^{j-k}$ in the Eq. A12.

For convenience, explicit h_{ℓ} for the smallest even chain lengths in the WBL are listed in Table I. These formulas

are useful because the supercurrent through lead ℓ can be computed by the Hellmann–Feynman theorem, which for zero temperature and zero chemical potential in the

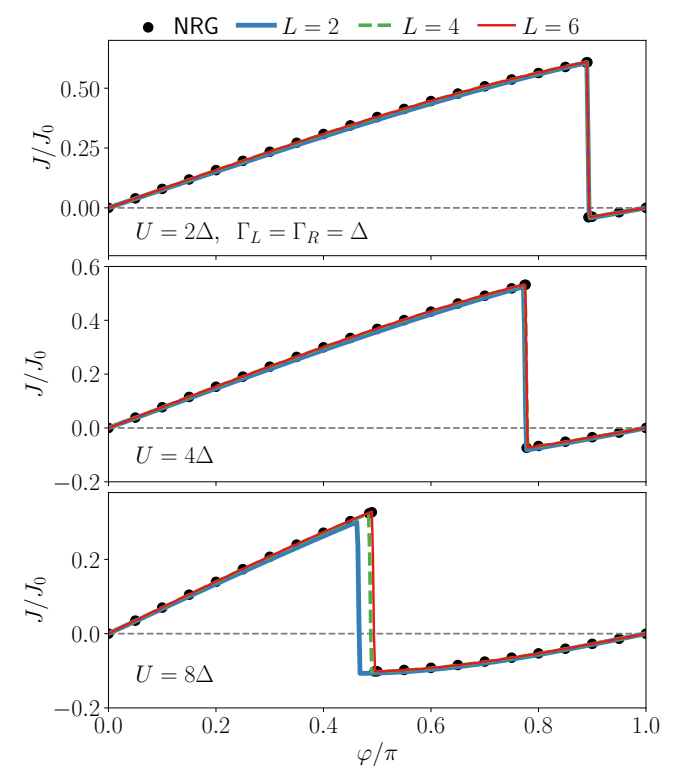


Figure 31. Single QD between two SC leads as illustrated in Fig. 5(b). Comparison of the supercurrent as a function of the Josephson phase for different U at half-filling ($\varepsilon=0$) between NRG (black circles) and single chain effective model sChE(L).

leads reads

$$J_{\ell} = \frac{2e}{\hbar} \frac{\partial E}{\partial \varphi_{\ell}} \tag{B4}$$

where E is the ground state energy.

Figure 31, which uses the same NRG data as Fig. 8, shows that a single chain suffices to capture the supercurrent, including the correct placement of current reversals associated with the underlying QPT. An even more interesting case is illustrated in the Fig. 10, which shows a three-terminal setup.

Appendix C: Non-interacting Green's function of a DOD

Consider the Hamiltonian of a parallel DQD connected to one SC lead. Following the procedure from the main text, we can write the Matsubara Green's function in the Nambu basis $\mathscr{D}^T=(d_{1\uparrow},d_{1\downarrow}^\dagger,d_{2\uparrow},d_{2\downarrow}^\dagger,c_{\mathbf{k}},c_{-\mathbf{k}}^\dagger),$

the factor χ , we have only the even L up to L					
L =	2	4	6	8	10
h_0	2	4	6	8	10
h_1	$2-\chi^2$	6 - χ^2	$\begin{array}{c} \frac{38 - 3\chi^2}{3} \\ -224 \end{array}$	$22-\chi^2$	$34-\chi^2$
h_2		$\frac{4}{6-\chi^2}$	$\frac{224}{3(38-3\chi^2)}$	$\frac{84}{22-\chi^2}$	$\frac{1056}{5(34-\chi^2)}$
h_3		$\frac{\frac{4}{6-\chi^2}}{\frac{8-8\chi^2+\chi^4}{6-\chi^2}}$	$\frac{3(172-116\chi^{2}+7\chi^{4})}{7(38-3\chi^{2})}$	$\frac{424 - 200\chi^2 + 7\chi^4}{7(22 - \chi^2)}$	$\frac{644 - 220\chi^2 + 5\chi^4}{5(34 - \chi^2)}$
h_4		$0-\chi$	$4(38-3\chi^{2})$	$176(22-\chi^2)$	$52(34-\chi^2)$
h_5			$\frac{7(172-116\chi^2+7\chi^4)}{7(32-48\chi^2+18\chi^4-\chi^6)}$	$\frac{\overline{21(424-200\chi^2+7\chi^4)}}{7(3440-3992\chi^2+1014\chi^4-33\chi^6)}$	$\frac{\overline{3(644-220\chi^2+5\chi^4)}}{5(9248-8624\chi^2+1554\chi^4-33\chi^6)}$
			$172 - 116\chi^2 + 7\chi^4$	$ \begin{array}{r} 33(424-200\chi^2+7\chi^4) \\ 4(424-200\chi^2+7\chi^4) \end{array} $	$\begin{array}{r} \hline 33(644 - 220\chi^2 + 5\chi^4) \\ 320(644 - 220\chi^2 + 5\chi^4) \\ \end{array}$
h_6				$11(3440-3992\chi^2+1014\chi^4-33\chi^6)$	$143(9248-8624\chi^2+1554\chi^4-33\chi^6)$
h_7				$\frac{33(128 - 256\chi^2 + 160\chi^4 - 32\chi^6 + \chi^8)}{3440 - 3992\chi^2 + 1014\chi^4 - 33\chi^6}$	$\frac{3(311232 - 509056\chi^2 + 244156\chi^4 - 34892\chi^6 + 715\chi^8)}{65(9248 - 8624\chi^2 + 1554\chi^4 - 33\chi^6)}$
h_8					$\frac{4(9248 - 8624\chi^2 + 1554\chi^4 - 33\chi^6)}{5(311232 - 509056\chi^2 + 244156\chi^4 - 34892\chi^6 + 715\chi^8)}$
h_9					$\frac{715(512 - 1280\chi^2 + 1120\chi^4 - 400\chi^6 + 50\chi^8 - \chi^{10})}{311232 - 500056\chi^2 + 244156\chi^4 - 34892\chi^6 + 715\chi^8}$

Table I. Chain-expansion coefficients for a block coupled to multiple leads, parameterized by the total coupling Γ_T and the geometric factor $\chi = \chi e^{i\Phi}$. We list only the even L up to L = 10.

$$G_{0}(i\omega_{n}, \mathbf{k})^{-1} = \begin{pmatrix} i\omega_{n} - \epsilon_{1} & 0 & -t_{d} & 0 & -V_{1\mathbf{k}} & 0\\ 0 & i\omega_{n} + \epsilon_{1} & 0 & t_{d} & 0 & V_{1\mathbf{k}} \\ -t_{d} & 0 & i\omega_{n} - \epsilon_{2} & 0 & -V_{2\mathbf{k}} & 0\\ 0 & t_{d} & 0 & i\omega_{n} + \epsilon_{2} & 0 & V_{2\mathbf{k}} \\ -V_{1\mathbf{k}} & 0 & -V_{2\mathbf{k}} & 0 & i\omega_{n} - \epsilon_{\mathbf{k}} & \Delta\\ 0 & V_{1\mathbf{k}} & 0 & V_{2\mathbf{k}} & \Delta & i\omega_{n} + \epsilon_{\mathbf{k}} \end{pmatrix},$$
(C1)

where we assume real $V_{j\mathbf{k}}$. We are interested in the im-

purity Green's function G_0^d . Following a standard blockmatrix inversion scheme (A1) we obtain a 4×4 matrix,

$$[G_0^d(i\omega_n)]^{-1} = \begin{pmatrix} i\omega_n - \epsilon_1 & 0 & -t_d & 0 \\ 0 & i\omega_n + \epsilon_1 & 0 & t_d \\ -t_d & 0 & i\omega_n - \epsilon_2 & 0 \\ 0 & t_d & 0 & i\omega_n + \epsilon_2 \end{pmatrix}$$

$$-\sum_{\mathbf{k}} \frac{1}{\omega_n^2 + \epsilon_{\mathbf{k}}^2 + \Delta^2} \begin{pmatrix} (i\omega_n + \epsilon_{\mathbf{k}})V_{1\mathbf{k}}^2 & \Delta V_{1\mathbf{k}}^2 & (i\omega_n + \epsilon_{\mathbf{k}})V_{1\mathbf{k}}V_{2\mathbf{k}} & \Delta V_{1\mathbf{k}}V_{2\mathbf{k}} \\ \Delta V_{1\mathbf{k}}^2 & (i\omega_n - \epsilon_{\mathbf{k}})V_{1\mathbf{k}}^2 & \Delta V_{1\mathbf{k}}V_{2\mathbf{k}} & (i\omega_n - \epsilon_{\mathbf{k}})V_{1\mathbf{k}}V_{2\mathbf{k}} \\ (i\omega_n + \epsilon_{\mathbf{k}})V_{1\mathbf{k}}V_{2\mathbf{k}} & \Delta V_{1\mathbf{k}}V_{2\mathbf{k}} & (i\omega_n + \epsilon_{\mathbf{k}})V_{2\mathbf{k}}^2 & \Delta V_{2\mathbf{k}}^2 \\ \Delta V_{1\mathbf{k}}V_{2\mathbf{k}} & (i\omega_n - \epsilon_{\mathbf{k}})V_{1\mathbf{k}}V_{2\mathbf{k}} & \Delta V_{2\mathbf{k}} & (i\omega_n - \epsilon_{\mathbf{k}})V_{2\mathbf{k}}^2 \end{pmatrix}.$$
(C2)

Assuming a constant DOS with half-bandwidth D, $\rho(\epsilon) = \Theta(|D-\epsilon|)/(2D)$, We rewrite the momentum summations as integrals,

This allows us to define real tunneling rates,

$$\Gamma_{ij}(\epsilon) = \pi \sum_{\mathbf{k}} V_{i\mathbf{k}} V_{j\mathbf{k}} \delta(\epsilon - \epsilon_{\mathbf{k}}) = \Gamma_{ij} \Theta(D - |\epsilon|) \quad (C4)$$

which are constant in WBL, $\Gamma_{ij}(\epsilon) = \Gamma_{ij}$ for $D \to \infty$. We denote

$$\widetilde{\Gamma}_{ij}(\omega_n) = \frac{\Gamma_{ij}}{\Delta} \widetilde{\Gamma}(\omega_n; D),$$
 where $\widetilde{\Gamma}(\omega_n; D)$ is given by Eq. (6). The inverse of the

impurity Green's function then reads

$$\sum_{\mathbf{k}} F(\epsilon_{\mathbf{k}}) = \frac{1}{2D} \int_{-D}^{D} d\epsilon F(\epsilon).$$
 (C3)

$$[G_0^d(i\omega_n)]^{-1} = \begin{bmatrix} i\omega_n[1+\widetilde{\Gamma}_{11}(\omega_n)] - \epsilon_1 & -\Delta\widetilde{\Gamma}_{11}(\omega_n) & i\omega_n\widetilde{\Gamma}_{21}(\omega_n) - t_d & -\Delta\widetilde{\Gamma}_{21}(\omega_n) \\ -\Delta\widetilde{\Gamma}_{11}(\omega_n) & i\omega_n[1+\widetilde{\Gamma}_{11}(\omega_n)] + \epsilon_1 & -\Delta\widetilde{\Gamma}_{21}(\omega_n) & i\omega_n\widetilde{\Gamma}_{21}(\omega_n) + t_d \\ i\omega_n\widetilde{\Gamma}_{12}(\omega_n) - t_d & -\Delta\widetilde{\Gamma}_{12}(\omega_n) & i\omega_n[1+\widetilde{\Gamma}_{22}(\omega_n)] - \epsilon_2 & -\Delta\widetilde{\Gamma}_{22}(\omega_n) \\ -\Delta\widetilde{\Gamma}_{12}(\omega_n) & i\omega_n\widetilde{\Gamma}_{12}(\omega_n) + t_d & -\Delta\widetilde{\Gamma}_{22}(\omega_n) & i\omega_n[1+\widetilde{\Gamma}_{22}(\omega_n)] + \epsilon_2 \end{bmatrix}.$$
(C6)

Appendix D: Technical details for numerical calculations

Most of the results presented in the main text using the ChE method were obtained via ED on standard PCs, employing various linear algebra routines from the SciPy package [100]. For longer chains, we used DMRG techniques implemented in the TenPy [101] and iTensor [102] libraries. The online examples published in Ref. [74] make use of the NetKet library [103, 104], owing to its

convenient representation of fermionic Hamiltonians and operators.

All NRG results were obtained using the open-source NRG Ljubljana package [105]. For single-channel problems (one chain), we used a logarithmic discretization parameter $\Lambda=2$, and for two-channel problems (two chains), we used $\Lambda=4$. Unless stated otherwise, the typical half-bandwidth was set to $D=100\Delta$, which effectively suppresses band-edge-related effects.

- S. De Franceschi, L. Kouwenhoven, C. Schönenberger, and W. Wernsdorfer, Hybrid superconductor-quantum dot devices, Nat. Nanotechnol. 5, 703 (2010).
- [2] B. W. Heinrich, J. I. Pascual, and K. J. Franke, Single magnetic adsorbates on s-wave superconductors, Prog. Surf. Sci. 93, 1 (2018).
- [3] M. Benito and G. Burkard, Hybrid superconductorsemiconductor systems for quantum technology, Appl. Phys. Lett. 116, 190502 (2020).
- [4] A. W. Draelos, M.-T. Wei, A. Seredinski, H. Li, Y. Mehta, K. Watanabe, T. Taniguchi, I. V. Borzenets, F. Amet, and G. Finkelstein, Supercurrent flow in multiterminal graphene Josephson junctions, Nano Lett. 19, 1039 (2020).
- [5] N. Pankratova, H. Lee, R. Kuzmin, K. Wickramasinghe, W. Mayer, J. Yuan, M. G. Vavilov, J. Shabani, and V. E. Manucharyan, Multiterminal Josephson effect, Phys. Rev. X 10, 031051 (2020).
- [6] J. C. Estrada Saldaña, A. Vekris, G. Steffensen, R. Žitko, P. Krogstrup, J. Paaske, K. Grove-Rasmussen, and J. Nygård, Supercurrent in a double quantum dot, Phys. Rev. Lett. 121, 257701 (2018).
- [7] J. C. Estrada Saldaña, A. Vekris, R. Žitko, G. Steffensen, P. Krogstrup, J. Paaske, K. Grove-Rasmussen, and J. Nygård, Two-impurity Yu-Shiba-Rusinov states in coupled quantum dots, Phys. Rev. B 102, 195143 (2020).
- [8] K. Grove-Rasmussen, G. Steffensen, A. Jellinggaard, M. H. Madsen, R. Zitko, J. Paaske, and J. Nygård, Yu-Shiba-Rusinov screening of spins in double quantum dots, Nat. Commun. 9, 2376 (2018).
- [9] A. Vekris, J. C. E. Saldaña, T. Kanne, M. Marnauza, D. Olsteins, F. Fan, X. Li, T. Hvid-Olsen, X. Qiu, H. Xu, J. Nygård, and K. Grove-Rasmussen, Josephson junctions in double nanowires bridged by in-situ deposited superconductors, Phys. Rev. Research 3, 033240 (2021).
- [10] G. O. Steffensen, J. C. E. Saldaña, A. Vekris, P. Krogstrup, K. Grove-Rasmussen, J. Nygård, A. L.

- Yeyati, and J. Paaske, Direct transport between superconducting subgap states in a double quantum dot, Phys. Rev. B **105**, L161302 (2022).
- [11] M. Ruby, B. W. Heinrich, Y. Peng, F. von Oppen, and K. J. Franke, Wave-function hybridization in Yu-Shiba-Rusinov dimers, Phys. Rev. Lett. 120, 156803 (2018).
- [12] D.-J. Choi, C. G. Fernández, E. Herrera, C. Rubio-Verdú, M. M. Ugeda, I. Guillamón, H. Suderow, J. I. Pascual, and N. Lorente, Influence of magnetic ordering between Cr adatoms on the Yu-Shiba-Rusinov states of the β-Bi₂Pd superconductor, Phys. Rev. Lett. 120, 167001 (2018).
- [13] A. Kamlapure, L. Cornils, J. Wiebe, and R. Wiesendanger, Engineering the spin couplings in atomically crafted spin chains on an elemental superconductor, Nat. Commun. 9, 3253 (2018).
- [14] S. Kezilebieke, M. Dvorak, T. Ojanen, and P. Liljeroth, Coupled Yu-Shiba-Rusinov states in molecular dimers on NbSe₂, Nano Lett. 18, 2311 (2018).
- [15] H. Ding, Y. Hu, M. T. Randeria, S. Hoffman, O. Deb, J. Klinovaja, D. Loss, and A. Yazdani, Tuning interactions between spins in a superconductor, Proc. Natl. Acad. Sci. 118, e2024837118 (2021).
- [16] P. Beck, L. Schneider, L. Rózsa, K. Palotás, A. Lászóffy, L. Szunyogh, J. Wiebe, and R. Wiesendanger, Spinorbit coupling induced splitting of Yu-Shiba-Rusinov states in antiferromagnetic dimers, Nat. Commun. 12, 2040 (2021).
- [17] F. Küster, S. Brinker, S. Lounis, S. S. P. Parkin, and P. Sessi, Long range and highly tunable interaction between local spins coupled to a superconducting condensate, Nat. Commun. 12, 6722 (2021).
- [18] H. Kim, A. Palacio-Morales, T. Posske, L. Rózsa, K. Palotás, L. Szunyogh, M. Thorwart, and R. Wiesendanger, Toward tailoring Majorana bound states in artificially constructed magnetic atom chains on elemental superconductors, Sci. Adv. 4, eaar5251 (2018).
- [19] E. Liebhaber, L. M. Rütten, G. Reecht, J. F. Steiner, S. Rohlf, K. Rossnagel, F. von Oppen, and K. J.

- Franke, Quantum spins and hybridization in artificially-constructed chains of magnetic adatoms on a superconductor, Nat. Commun. 13, 2160 (2022).
- [20] C. Li, V. Pokorný, M. Žonda, J.-C. Liu, P. Zhou, O. Chahib, T. Glatzel, R. Häner, S. Decurtins, S.-X. Liu, R. Pawlak, and E. Meyer, Individual assembly of radical molecules on superconductors: Demonstrating quantum spin behavior and bistable charge rearrangement, ACS Nano 19, 3403 (2025).
- [21] J.-C. Liu, C. Li, O. Chahib, X. Wang, S. Rothenbühler, R. Häner, S. Decurtins, U. Aschauer, S.-X. Liu, E. Meyer, and R. Pawlak, Spin excitations of high spin iron(II) in metal-organic chains on metal and superconductor, Adv. Sci. 12, 2412351 (2025).
- [22] C. Li, V. Pokorný, P. Hapala, M. Žonda, P. Zhou, S. Decurtins, S.-X. Liu, F. Song, R. Pawlak, and E. Meyer, Negative differential conductance in triangular molecular assemblies (2025), arXiv:2508.05575 [cond-mat.meshall].
- [23] S. Trivini, J. Ortuzar, J. Zaldivar, E. Herrera, I. Guillamón, H. Suderow, F. S. Bergeret, and J. I. Pascual, Diluted Yu-Shiba-Rusinov arrays on the anisotropic superconductor β-Bi₂Pd, Phys. Rev. B 110, 235405 (2024).
- [24] G. O. Steffensen and A. L. Yeyati, Yu-Shiba-Rusinov– bond qubit in a double quantum dot with circuit-QED operation, PRX Quantum 6, 020329 (2025).
- [25] J. Zaldívar, J. Ortuzar, M. Alvarado, S. Trivini, J. Baumard, C. Rubio-Verdú, E. Herrera, H. Suderow, A. L. Yeyati, F. S. Bergeret, and J. I. Pascual, Revealing band-hybrid Cooper pairs on the surface of a superconductor with spin-orbit coupling, Phys. Rev. Lett. 135, 136201 (2025).
- [26] L. Lakic, W. I. L. Lawrie, D. van Driel, L. E. A. Ste-houwer, Y. Su, M. Veldhorst, G. Scappucci, F. Kuemmeth, and n. Chatterjee, A quantum dot in germanium proximitized by a superconductor, Nat. Mater. 24, 552 (2025).
- [27] V. Meden, The Anderson-Josephson quantum dot—a theory perspective, J. Phys. Condens. Matter 31, 163001 (2019).
- [28] T. Iličin and R. Žitko, Variational solution of the superconducting Anderson impurity model and the bandedge singularity phenomena, SciPost Phys. 19, 006 (2025).
- [29] A. Keliri and M. Schiró, Slave-spin approach to the Anderson-Josephson quantum dot (2025), arXiv:2502.14843 [cond-mat.mes-hall].
- [30] C. P. Moca, I. Weymann, M. A. Werner, and G. Zaránd, Kondo cloud in a superconductor, Phys. Rev. Lett. 127, 186804 (2021).
- [31] A. Keliri and B. Douçot, Driven Andreev molecule, Phys. Rev. B 107, 094505 (2023).
- [32] J. Cheng, X. Zuo, J. Wang, and Y. Xing, Quasiparticle trapping in quench dynamics of superconductor/quantum dot/superconductor Josephson junctions, Phys. Rev. B 110, 125417 (2024).
- [33] R. Žitko, Numerical subgap spectroscopy of double quantum dots coupled to superconductors, Phys. Rev. B 91, 165116 (2015).
- [34] M. Žonda, P. Zalom, T. Novotný, G. Loukeris, J. Bätge, and V. Pokorný, Generalized atomic limit of a double quantum dot coupled to superconducting leads, Phys. Rev. B 107, 115407 (2023).
- [35] P. Zalom, K. Wrześniewski, T. Novotný, and I. Wey-

- mann, Double quantum dot Andreev molecules: Phase diagrams and critical evaluation of effective models, Phys. Rev. B **110**, 134506 (2024).
- [36] A. Kadlecová, M. Žonda, and T. Novotný, Quantum dot attached to superconducting leads: Relation between symmetric and asymmetric coupling, Phys. Rev. B 95, 195114 (2017).
- [37] A. Kadlecová, M. Žonda, V. Pokorný, and T. Novotný, Practical guide to quantum phase transitions in quantum-dot-based tunable Josephson junctions, Phys. Rev. Appl. 11, 044094 (2019).
- [38] P. Zalom, M. Zonda, and T. Novotný, Hidden symmetry in interacting-quantum-dot-based multiterminal Josephson junctions, Phys. Rev. Lett. 132, 126505 (2024).
- [39] M. Geier, R. S. Souto, J. Schulenborg, S. Asaad, M. Leijnse, and K. Flensberg, Fermion-parity qubit in a proximitized double quantum dot, Phys. Rev. Research 6, 023281 (2024).
- [40] R. Bulla, T. A. Costi, and T. Pruschke, Numerical renormalization group method for quantum impurity systems, Rev. Mod. Phys. 80, 395 (2008).
- [41] T. Yoshioka and Y. Ohashi, Numerical renormalization group studies on single impurity Anderson model in superconductivity: A unified treatment of magnetic, nonmagnetic impurities, and resonance scattering, J. Phys. Soc. Jpn. 69, 1812 (2000).
- [42] J. Bauer, A. Oguri, and A. C. Hewson, Spectral properties of locally correlated electrons in a Bardeen–Cooper– Schrieffer superconductor, J. Phys.: Condens. Matter 19, 486211 (2007).
- [43] N. Y. Yao, C. P. Moca, I. Weymann, J. D. Sau, M. D. Lukin, E. A. Demler, and G. Zaránd, Phase diagram and excitations of a Shiba molecule, Phys. Rev. B 90, 241108 (2014).
- [44] R. Žitko, Spectral properties of Shiba subgap states at finite temperatures, Phys. Rev. B 93, 195125 (2016).
- [45] P. Zalom, V. Pokorný, and T. Novotný, Spectral and transport properties of a half-filled Anderson impurity coupled to phase-biased superconducting and metallic leads, Phys. Rev. B 103, 035419 (2021).
- [46] P. Zalom and T. Novotný, Tunable reentrant Kondo effect in quantum dots coupled to metal-superconducting hybrid reservoirs, Phys. Rev. B 104, 035437 (2021).
- [47] P. Zalom, Rigorous Wilsonian renormalization group for impurity models with a spectral gap, Phys. Rev. B 108, 195123 (2023).
- [48] F. Siano and R. Egger, Josephson current through a nanoscale magnetic quantum dot, Phys. Rev. Lett. 93, 047002 (2004).
- [49] D. J. Luitz and F. F. Assaad, Weak-coupling continuous-time quantum Monte Carlo study of the single impurity and periodic Anderson models with s-wave superconducting baths, Phys. Rev. B 81, 024509 (2010).
- [50] D. J. Luitz, F. F. Assaad, T. Novotný, C. Karrasch, and V. Meden, Understanding the Josephson current through a Kondo-correlated quantum dot, Phys. Rev. Lett. 108, 227001 (2012).
- [51] V. Pokorný and M. Žonda, Correlation effects in superconducting quantum dot systems, Physica B: Condens. Matter 536, 488 (2018).
- [52] V. Pokorný and T. Novotný, Footprints of impurity quantum phase transitions in quantum Monte Carlo statistics, Phys. Rev. Research 3, 023013 (2021).

- [53] A. L. Yeyati, J. C. Cuevas, A. López-Dávalos, and A. Martín-Rodero, Resonant tunneling through a small quantum dot coupled to superconducting leads, Phys. Rev. B 55, R6137 (1997).
- [54] A. Martin-Rodero, A. Levy Yeyati, and J. C. Cuevas, General transport properties of superconducting quantum point contacts: a Green functions approach, Superlattices Microstruct. 25, 925 (1999).
- [55] A. Martín-Rodero and A. Levy Yeyati, Josephson and Andreev transport through quantum dots, Adv. Phys. 60, 899 (2011).
- [56] A. Ptok, S. Głodzik, and T. Domański, Yu-Shiba-Rusinov states of impurities in a triangular lattice of NbSe₂ with spin-orbit coupling, Phys. Rev. B 96, 184425 (2017).
- [57] A. T. Alastalo, R. J. Joynt, and M. M. Salomaa, The Anderson model in a superconductor: Φ-derivable theory, J. Phys. Condens. Matter 10, L63 (1998).
- [58] E. Vecino, A. Martín-Rodero, and A. L. Yeyati, Josephson current through a correlated quantum level: Andreev states and π junction behavior, Phys. Rev. B **68**, 035105 (2003).
- [59] T. Meng, S. Florens, and P. Simon, Self-consistent description of Andreev bound states in Josephson quantum dot devices, Phys. Rev. B 79, 224521 (2009).
- [60] M. Žonda, V. Pokorný, V. Janiš, and T. Novotný, Perturbation theory of a superconducting $0-\pi$ impurity quantum phase transition, Sci. Rep. 5, 8821 (2015).
- [61] M. Žonda, V. Pokorný, V. Janiš, and T. Novotný, Perturbation theory for an Anderson quantum dot asymmetrically attached to two superconducting leads, Phys. Rev. B 93, 024523 (2016).
- [62] C. Karrasch, A. Oguri, and V. Meden, Josephson current through a single Anderson impurity coupled to BCS leads, Phys. Rev. B 77, 024517 (2008).
- [63] N. Wentzell, S. Florens, T. Meng, V. Meden, and S. Andergassen, Magnetoelectric spectroscopy of Andreev bound states in Josephson quantum dots, Phys. Rev. B 94, 085151 (2016).
- [64] V. Pokorný and M. Žonda, Effective low-energy models for superconducting impurity systems, Phys. Rev. B 107, 155111 (2023).
- [65] V. V. Baran, E. J. P. Frost, and J. Paaske, Surrogate model solver for impurity-induced superconducting subgap states, Phys. Rev. B 108, L220506 (2023).
- [66] V. V. Baran and J. Paaske, Bcs surrogate models for floating superconductor-semiconductor hybrids, Phys. Rev. B 109, 224501 (2024).
- [67] R. S. Souto, V. V. Baran, M. Nitsch, L. Maffi, J. Paaske, M. Leijnse, and M. Burrello, Majorana modes in quantum dots coupled via a floating superconducting island, Phys. Rev. B 111, 174501 (2025).
- [68] A. W. Chin, A. Rivas, S. F. Huelga, and M. B. Plenio, Exact mapping between system-reservoir quantum models and semi-infinite discrete chains using orthogonal polynomials, J. Math. Phys. 51, 092109 (2010).
- [69] E. Arrigoni, M. Knap, and W. von der Linden, Nonequilibrium dynamical mean-field theory: An auxiliary quantum master equation approach, Phys. Rev. Lett. 110, 086403 (2013).
- [70] A. Dorda, M. Nuss, W. von der Linden, and E. Arrigoni, Auxiliary master equation approach to nonequilibrium correlated impurities, Phys. Rev. B 89, 165105 (2014).
- [71] F. Schwarz, M. Goldstein, A. Dorda, E. Arrigoni,

- A. Weichselbaum, and J. von Delft, Lindblad-driven discretized leads for nonequilibrium steady-state transport in quantum impurity models: Recovering the continuum limit, Phys. Rev. B **94**, 155142 (2016).
- [72] J. B. Rigo and A. K. Mitchell, Unsupervised learning of effective quantum impurity models, Phys. Rev. Res. 6, 043044 (2024).
- [73] J. B. Rigo and A. K. Mitchell, Machine learning effective models for quantum systems, Phys. Rev. B 101, 241105 (2020).
- [74] M. Žonda and D. Bobok, Chain Expansion for SC nanostructures, https://gitlab.mff.cuni.cz/zondam/chain-expansion (2025).
- [75] K. S. D. Beach, R. J. Gooding, and F. Marsiglio, Reliable Padé analytical continuation method based on a high-accuracy symbolic computation algorithm, Phys. Rev. B 61, 5147 (2000).
- [76] Ž. Osolin and R. Žitko, Padé approximant approach for obtaining finite-temperature spectral functions of quantum impurity models using the numerical renormalization group technique, Phys. Rev. B 87, 245135 (2013).
- [77] J. Schött, I. L. M. Locht, E. Lundin, O. Gräs, O. Eriksson, and I. Di Marco, Analytic continuation by averaging Padé approximants, Phys. Rev. B 93, 075104 (2016).
- [78] J. Fei, C.-N. Yeh, and E. Gull, Nevanlinna analytical continuation, Phys. Rev. Lett. 126, 056402 (2021).
- [79] J. Hu, R.-X. Xu, and Y. Yan, Communication: Padé spectrum decomposition of Fermi function and Bose function, J. Chem. Phys. 133, 101106 (2010).
- [80] J. Hu, M. Luo, F. Jiang, R.-X. Xu, and Y. Yan, Padé spectrum decompositions of quantum distribution functions and optimal hierarchical equations of motion construction for quantum open systems, J. Chem. Phys. 134, 244106 (2011).
- [81] R. Smorka, M. Thoss, and M. Žonda, Dynamics of spin relaxation in nonequilibrium magnetic nanojunctions, New J. Phys. 26, 013056 (2024).
- [82] G. A. Baker and P. Graves-Morris, Padé approximants, 2nd ed., Encyclopedia of mathematics and its applications (Cambridge University Press, Cambridge, England, 1996).
- [83] H. S. Wall, Analytic theory of continued fractions (Courier Dover Publications, 2018).
- [84] F. Eickhoff, B. Lechtenberg, and F. B. Anders, Effective low-energy description of the two-impurity Anderson model: RKKY interaction and quantum criticality, Phys. Rev. B 98, 115103 (2018).
- [85] P. Zalom, D. Rolih, and R. Žitko, Andreev bound state spectroscopy of a quantum-dot-based Aharonov-Bohm interferometer with superconducting terminals (2025), arXiv:2507.03614 [cond-mat.mes-hall].
- [86] B. Baran, R. Taranko, and T. Domański, Subgap dynamics of double quantum dot coupled between superconducting and normal leads, Sci. Rep. 11, 11138 (2021).
- [87] R. Žitko, M. Lee, R. López, R. Aguado, and M.-S. Choi, Josephson current in strongly correlated double quantum dots, Phys. Rev. Lett. 105, 116803 (2010).
- [88] M. Lee, T. Jonckheere, and T. Martin, Josephson effect through a multilevel quantum dot near a singlet-triplet transition, Phys. Rev. B 81, 155114 (2010).
- [89] C. Karrasch, S. Andergassen, and V. Meden, Supercurrent through a multilevel quantum dot close to singlet-triplet degeneracy, Phys. Rev. B 84, 134512 (2011).

- [90] C. Ortega-Taberner, A.-P. Jauho, and J. Paaske, Anomalous Josephson current through a driven double quantum dot, Phys. Rev. B 107, 115165 (2023).
- [91] C. Plorin and M. Potthoff, Kondo screening and indirect magnetic exchange through a conventional superconductor studied by the density matrix renormalization group, Phys. Rev. B 110, 085119 (2024).
- [92] Á. Bácsi, L. Pavešić, and R. Žitko, Exchange interaction between two quantum dots coupled through a superconducting island, Phys. Rev. B 108, 115160 (2023).
- [93] R. Žitko and J. Bonča, Multiple-impurity Anderson model for quantum dots coupled in parallel, Phys. Rev. B 74, 045312 (2006).
- [94] S. Körber, B. Trauzettel, and O. Kashuba, Collective Yu-Shiba-Rusinov states in magnetic clusters at superconducting surfaces, Phys. Rev. B 97, 184503 (2018).
- [95] L. M. Rütten, H. Schmid, E. Liebhaber, G. Franceschi, A. Yazdani, G. Reecht, K. Rossnagel, F. von Oppen, and K. J. Franke, Wave function engineering on superconducting substrates: Chiral Yu-Shiba-Rusinov molecules, ACS Nano 18, 30798 (2024).
- [96] E. Siuda and I. Weymann, Competition between Nagaoka ferromagnetism and superconducting pairing in hybrid quantum dots, Sci. Rep. 15, 25349 (2025).
- [97] P. W. Anderson, More is different, Science 177, 393 (1972).
- [98] V. Pokorný and P. Ram, Evolution of the Andreev bands in the half-filled superconducting periodic Anderson model, Phys. Rev. B 104, 155102 (2021).
- [99] T.-T. Lu and S.-H. Shiou, Inverses of 2×2 block matrices, Comput. Math. Appl. 43, 119 (2002).
- [100] P. Virtanen, R. Gommers, T. E. Oliphant, M. Haberland, T. Reddy, D. Cournapeau, E. Burovski, P. Pe-

- terson, W. Weckesser, J. Bright, S. J. van der Walt, M. Brett, J. Wilson, K. J. Millman, N. Mayorov, A. R. J. Nelson, E. Jones, R. Kern, E. Larson, C. J. Carey, İ. Polat, Y. Feng, E. W. Moore, J. VanderPlas, D. Laxalde, J. Perktold, R. Cimrman, I. Henriksen, E. A. Quintero, C. R. Harris, A. M. Archibald, A. H. Ribeiro, F. Pedregosa, P. van Mulbregt, and SciPy 1.0 Contributors, SciPy 1.0: Fundamental Algorithms for Scientific Computing in Python, Nat. Methods 17, 261 (2020).
- [101] J. Hauschild, J. Unfried, S. Anand, B. Andrews, M. Bintz, U. Borla, S. Divic, M. Drescher, J. Geiger, M. Hefel, K. Hémery, W. Kadow, J. Kemp, N. Kirchner, V. S. Liu, G. Möller, D. Parker, M. Rader, A. Romen, S. Scalet, L. Schoonderwoerd, M. Schulz, T. Soejima, P. Thoma, Y. Wu, P. Zechmann, L. Zweng, R. S. K. Mong, M. P. Zaletel, and F. Pollmann, Tensor network Python (TeNPy) version 1, SciPost Phys. Codebases, 41 (2024).
- [102] M. Fishman, S. R. White, and E. M. Stoudenmire, The ITensor Software Library for Tensor Network Calculations, SciPost Phys. Codebases, 4 (2022).
- [103] G. Carleo, K. Choo, D. Hofmann, J. E. Smith, T. Westerhout, F. Alet, E. J. Davis, S. Efthymiou, I. Glasser, S.-H. Lin, M. Mauri, G. Mazzola, C. B. Mendl, E. van Nieuwenburg, O. O'Reilly, H. Théveniaut, G. Torlai, F. Vicentini, and A. Wietek, NetKet: A machine learning toolkit for many-body quantum systems, SoftwareX, 100311 (2019).
- [104] F. Vicentini, D. Hofmann, A. Szabó, D. Wu, C. Roth, C. Giuliani, G. Pescia, J. Nys, V. Vargas-Calderón, N. Astrakhantsev, and G. Carleo, NetKet 3: Machine learning toolbox for many-body quantum systems, Sci-Post Phys. Codebases, 7 (2022).
- [105] R. Žitko, NRG Liubliana, Zenodo (2021).